Peer-reviewed version available at Remote Sens. 2019, 11, 3045; doi:10.3390/rs11243045

Article

A Study of Characteristics of Warm Cloud-precipitation in South China during the Pre-flood Season Using Datasets Observed from a Cloud Radar, Ceilometer, and Disdrometer

Jiafeng Zheng [1*], Liping Liu [2], Haonan Chen [3], Yabin Gou [4], Yuzhang Che [1,5], Haolin Xu [1], and Qian Li [1]

[1] Plateau Atmosphere and Environment Key Laboratory of Sichuan Province, School of Atmospheric Sciences, Chengdu University of Information Technology, Chengdu 610225, China; zjf1988@cuit.edu.cn (J. Z.); cyz@cuit.edu.cn (Y.C.) 3170101064@cuit.edu.cn (H.X.); 3170101067@cuit.edu.cn (Q.L.)
[2] State Key Lab of Severe Weather, Chinese Academy of Meteorological Sciences, Beijing 100081, China; liulp@cma.gov.cn (L.L.)
[3] NOAA/Earth System Research Laboratory, Boulder, CO 80305, USA; haonan.chen@noaa.gov (H.C.)
[4] Hangzhou Meteorological Bureau, Hangzhou 310051, China; 2017011201@cuit.edu.cn (Y.G.)
[5] Department of Mechanical Engineering, Tokyo Institute of Technology, Ookayama, Meguro-ku, Tokyo 152-8550, Japan
* Correspondence: zjf1988@cuit.edu.cn;

Abstract: Warm cloud-precipitation plays a vital role in the hydrological cycle, weather, and climate. Comprehensive observation and study of warm cloud-precipitation can advance our understanding of the internal physical processes and provide valuable information for developing the numerical models. This paper mainly focused on a study of characteristics of warm cloud-precipitation in South China during the pre-flood season using datasets observed from a Ka-band cloud radar, laser ceilometer and disdrometer. Eighteen kinds of quantities from these three instruments were used to precisely elucidate the distribution, diurnal variation, vertical structure, and physical property of warm cloud-precipitation. The results showed that the occurrence of aloft cloud-precipitation decreased with the increase of height, and most of the hydrometeors were distributed below 2 km. During the observation period, the ground rainfall mainly came from light precipitation; however, short-time and sharp showers contributed to the majority of rain amounts. Most of the cloud layers were single-layer, with base heights below 2.2 km, thickness thinner than 2.1 km, and top heights within 0.6-4.2 km. Warm cloud-precipitation owned certain diurnal variations, with a rising trend of cloud base heights in the afternoon and midnight. During 0230-1100, 1200-1800, and 2100-2300, the convections were relatively active with higher cloud tops, thicker cloud thickness, and higher rainfall occurrences. Separation and statistical results of cloud and precipitation indicated that they owned different vertical structures and physical properties, exhibiting different value ranges and changes of radar reflectivity, vertical air motion, particle size, number concentration, liquid water, and rain rate at different height levels. The particle size distributions of cloud and precipitation both were exponential. Radar-derived raindrop size distribution was very coherent with the ground measurement when the reflectivity of precipitation was within 10-20 dBZ. However, for other reflectivity regimes, instrument sensitivity, sampling height, attenuation, and non-precipitating weak targets can affect the comparison.

Keywords: warm cloud-precipitation; cloud radar; ceilometer; disdrometer; South China;

1. Introduction

Peer-reviewed version available at Remote Sens. 2019, 11, 3045; doi:10.3390/rs11243045

Warm cloud-precipitation consisting of liquid hydrometeors through condensation, collision, and coalescence processes [1], lies in the low level of atmosphere. It covers a large part of the earth's surface and thus directly affects the global hydrological cycle, energy budget, and climate [2,3]. Warm cloud-precipitation also can adjust the atmosphere stability and provide sufficient energy and water vapor for the formation and development of the convection systems [4]. Exceptional detection and study of warm cloud-precipitation by remote sensing can be valuable ways to promote our understanding of the concerned cloud-precipitation physical and dynamic issues, provide valuable information for current numerical weather and climate models, and also help conduct realistic missions of weather modification.

In recent years, radiosonde, aircraft, satellite, and ground-based remote sensing techniques have been used to observe and study the cloud-precipitation with certain purposes under specific scientific backgrounds [5-8]. The radiosonde is usually used to obtain in-situ measurements of temperature, relative humidity, wind, and pressure profiles. Those measurements can be utilized to estimate the vertical structures of the cloud, such as cloud base height, cloud top height, cloud layer number, and cloud thickness, as balloons penetrate the cloud layers [9-12]. Nevertheless, the number of radiosonde stations is relatively limited, and each radiosonde can only be operated twice per day, which largely limits the observation of the cloud in both temporal and spatial space. [13,14]. Aircraft carries sensors that typically yield a detailed description of the horizontal structure of cloud-precipitation and also can obtain the hydrometeor properties in the vertical direction by making multiple passes at different height levels [15,16]. Compared with other sounding means, aircraft penetration is a more reliable way for the sophisticated detection of cloud-inner properties. It provides plenty of high-quality microphysical and dynamic quantities, such as particle size, particle number concentration, hydrometeor type, hydrometeor phase, water content, and vertical air motion, which are very valuable for the study of cloud-precipitation physical issues [17,18]. However, aircraft penetration is very costly and can only provide instantaneous measurements during a specific period and over particular regions; thus, it is not the optimal choice for the long-term or the large-regional observation of cloud-precipitation [19]. Satellites equipped with passive and active remote sensors have nearly become a development tendency of the atmosphere sounding due to its significant advantage in the spatial coverage. They can provide data without any topographic limitations, especially over oceans and plateaus, where are difficult for other technologies to achieve [20]. For instance, geostationary satellites like Himawari series, Geostationary Operational Environmental Satellite (GOES) series, Fengyun-2 (FY-2) series, and Fengyun-4A (FY-4A) can offer real-time cloud maps over the fixed areas with large regional coverages and provide multispectral measurements, including cloud top height, cloud temperature, cloud types, cloud movement, and et al. These measurements play key roles in weather forecasting and severe weather monitoring [21-24]. Nonetheless, the spatial and temporal resolutions of geostationary satellites are still relatively low and can hardly satisfy the request of the fine-scale observation and research of cloud-precipitation [25]. Besides, due to the shallow and small-scale characteristics, the low-level warm cloud-precipitation often reflects similar radiation properties as the ground targets, leading uncertainties and retrieval biases existed in the corresponding products of geostationary satellites [26,27]. As a contrast, polar-orbiting satellites can be more prevalently used in cloud-precipitation vertical detection, especially when they equip with meteorological radars, such as the Tropical Rainfall Measuring Mission (TRMM), Cloudsat, Cloud-Aerosol Lidar and Infrared Pathfinder Satellite Observations (CALIPSO), and Global Precipitation Measurement (GPM) [28-30]. These on-board radars are designed with high sensitivities and spatial resolutions to ensure the capability of detecting weak meteorological targets, such as non-precipitating clouds and aerosols. They can profile the nether cloud layers as satellites moving in orbits, and obtain many precise measurements, including radar reflectivity, hydrometeor type, particle number concentration, water content, rain rate, and et al. [31-35]. These measurements have been applied in many atmospheric science fields, such as evaluating the cloud radiative effect and their influence on regional and global climate, investigating the features of high-impact severe weather systems, revealing the physical features of different cloud-precipitation types, and elucidating vertical structures of cloud-precipitation in specific regions [36-39]. Although the satellite-based radars have been widely used,

Peer-reviewed version available at Remote Sens. 2019, 11, 3045; doi:10.3390/rs11243045

there are some deficiencies of those radars for warm cloud-precipitation detection. First, as moving along with satellites, the spaceborne radar only profiles cloud layers in the same regions with limited times per day, which lead to time discontinuity of measurements. Thus, they cannot supply the in-situ study of the diurnal variation of cloud-precipitation. Second, in low altitude, spaceborne radars tend to suffer from the contamination of surface clutter, for which the radar signals are wholly invalid. For instance, the lowest three or four bins in the profile of radar on Cloudsat are invalid, leading to the incapability of cloud detection below 1 km, which is a sizeable blind altitude and can cause the incomplete detection of a large part of warm cloud-precipitation [40,41].

In the continental region, ground-based remote sensing technologies, such as millimeter-wave cloud radar (MMCR), laser ceilometer, and disdrometer, can be better alternatives for the long-term in-situ observation of cloud-precipitation. The MMCR typically involves Ka-band and W-band with wavelengths of ~8 mm and ~3 mm, respectively. These short-wavelength radars own a high-sensitivity ability to detect the small particle in weak cloud layers, such as cirrus, small-scale cumulus, and low-level stratiform cloud, because of the scattered ability of a hydrometer is inversely proportional to the fourth power of the electromagnetic wavelength [42-45]. By operating in the vertically pointing mode with the transmission of narrow pulses, MMCRs also have very high spatial and temporal resolutions, which are only a few decameters and seconds. That means the radars can continuously profile the aloft cloud-precipitation in a short-time interval and provide subtle vertical observations. MMCRs can provide not only target reflectivity but also Doppler velocity and spectrum, based on which many macro- and microphysical quantities of cloud-precipitation can be further obtained by using specific retrieval methods [46]. Due to its continuous observation capability, ground-based MMCRs have been used in many significant science programs in many countries, such as the Atmospheric Radiation Measurement (ARM) projects in the USA, the Third Tibetan Plateau Atmospheric Science Experiment (TIPEX-III) in China, and the Cloudnet in Europe [47-49]. However, it is a remarkable fact that the MMCR is generally deployed in conjunction with other instruments, such as ceilometer and disdrometer, because it suffers from attenuation and is incapable of detecting the cloud base height under precipitating conditions. In contrast, the ceilometer can provide accurate cloud base height in the low-level atmosphere, and the disdrometer can offer sophisticated rainfall and raindrop information; therefore, these two instruments can be the complements [50,51]. Previous studies have proposed that the comprehensive observation of these instruments can provide more confident and high-quality data sources for elucidating the cloud-precipitation diurnal variations, vertical structures, and cloud-precipitation physical properties [25,52,53].

South China is one of the moistest regions of mainland China. Under influences of pacific subtropical high, East Asian monsoon, shear line system, and front action, plenty of cloud-precipitation events are happened in this region during the pre-flood season from April to June to account for 40-50% of the annual rain amount [54]. For cloud-precipitation observation in South China, despite an S-band weather radar network and many weather stations have been constructed for severe weather monitoring, the cloud-precipitation observation in the vertical detection is still lack of capability. As a consequence, in 2016, a scientific experiment was carried out by Chinese Academy of Meteorological Sciences and other institutions, the experiment deployed the Ka-band MMCR, laser ceilometer, laser ceilometer, radiometer, wind profiler, and C-band vertically pointing radar in Longmen site of Guangdong province, to constitute a suite of vertical observation system for cloud and precipitation [55]. Based on the experiment observation, vertical structures, raindrop size distribution, and microphysical properties of different convection types have been studied by some scientists [25,56,57]. However, specific researches on the warm cloud-precipitation have not been investigated yet. Besides, according to the statistical result from MMCR, a large part of hydrometeors are concentrated in the low altitude in this region, indicating the warm cloud-precipitation can account for a large occurrence of the entire cloud-precipitation events [25].

The main purpose of this paper is to investigate the diurnal variation, vertical structure, and macro- and microphysical properties of warm cloud-precipitation in South China during the pre-flood season in 2016, using the long-term measurements of Ka-band MMCR, laser ceilometer, and disdrometer. The remainder of the paper is organized as follows. Section 2 presents detailed

Peer-reviewed version available at Remote Sens. 2019, 11, 3045; doi:10.3390/rs11243045

descriptions of the three instruments, data processing and quality control technologies, and warm cloud-precipitation determination and physical quantity retrieval methods. Section 3 provides the results of data quality control and analyzes the general characteristics, diurnal variation, vertical structure, and particle size distribution of warm cloud-precipitation. Section 4 makes a discussion of the differences between the radar-derived results and disdrometer measurements. Section 5 ends the paper with a summary.

2. Materials and Methods

2.1. Instruments and measurements

During the experiment period from 14 April to 18 June in 2016, the Ka-band MMCR, ceilometer, and disdrometer, were simultaneously deployed at Longmen weather observatory (LM, 23.783°N, 114.25°E, 86 m above sea level) of Guangdong Province, a coastal site near the Pearl River Delta of China. The three instruments were expected to provide continuous, long-term and high-resolution measurements of cloud-precipitation over the site. The experiment location and equipment appearance are shown in Figure 1.

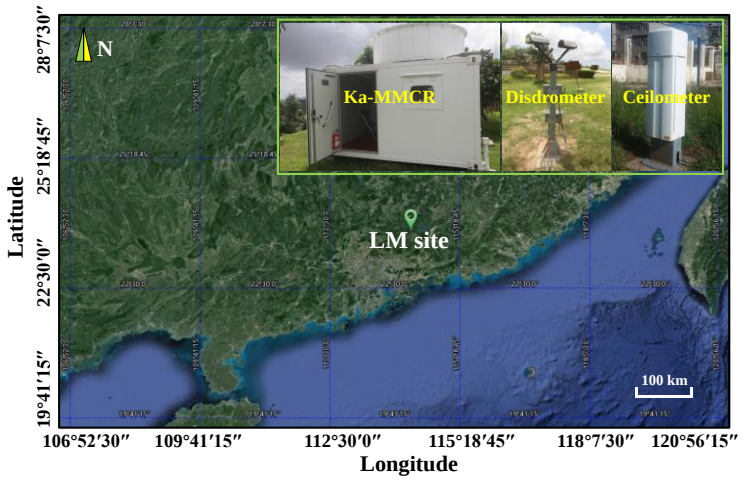

Figure 1. Experiment location of Longmen weather observatory (LM, 23.783°N, 114.25°E, 86 m above sea level), and appearance of the Ka-band MMCR, disdrometer, and ceilometer.

2.1.1. Ka-band MMCR

The Ka-band MMCR is a Doppler, solid-state and polarimetric radar. It works at 33.44 GHz, with a wavelength of 8.9 mm and a peak power over 100 W. By operating in a vertically pointing mode, the radar can continuously observe vertical profiles of Doppler spectrum (SP), radar reflectivity (Z, dBZ), mean Doppler velocity (V_M, $m \cdot s^{-1}$), spectrum width (S_w, $m \cdot s^{-1}$), and linear depolarization ratio (LDR, dB) of cloud-precipitation over the site, with a spatial resolution of 30 m and a temporal resolution of ~9 s. To largely meet the requirement of cloud-precipitation observation at different heights with different intensities, multiple radar operational modes were designed by configuring with different radar parameters and signal processing technologies. Detailed descriptions of their differences can be found in previous work [58]. Herein, for the sake of the study of warm cloud-precipitation, measurements observed by radar precipitation mode were used. Table 1 presents the main technical parameters of the MMCR and precipitation mode.

Table 1. The main technical parameters of the MMCR and precipitation mode.

MMCR and M3	Items	Technical Specifications
Radar system	Frequency (Wavelength)	33.44 GHz (8.9 mm)
	Transmitted peak power	≥ 100 W
	Beam width	0.3 degree

Peer-reviewed version available at Remote Sens. 2019, 11, 3045; doi:10.3390/rs11243045

Radar precipitation mode	Pulse repetition frequency	8333 Hz
	Gate number	510
	Vertical resolution	30 m
	Horizontal resolution	26 m at 5km
	Temporal resolution	~9 s
	Transmitted pulse width	0.2 μs
	Spectrum bin number	256
	Detectable height range	150 – 15.3 km
	Detectable reflectivity range	-33 – 30 dBZ
	Detectable velocity range	-18.67 – 18.67 m s^{-1}
	Spectrum velocity resolution	0.145 m s^{-1}
	Measurements	Doppler spectrum, reflectivity, mean Doppler velocity, spectrum width, and linear depolarization ratio

2.1.2. Ceilometer and disdrometer

The ceilometer was made by Vaisala company (Finland) and designed using a pulsed diode laser Light Detection and Ranging (LIDAR) technology. It emits laser pulse in a vertical direction and receives the backscattered signal reflected from the cloud, precipitation, or other targets. The ceilometer provides backscatter profile and cloud base height, with a vertical resolution of 10 m and a temporal resolution of 2-3 s. The disdrometer was made by OTT Hydromet company (Germany). It equips a laser-optical transmitter that can simultaneously detect the particle size and falling speed based on signal attenuation caused by the passing hydrometeor. The measuring height is 1.4 m above the ground, and the sampling time is 60 s. The diameter and velocity information of hydrometeor were recorded by division into 32 non-equidistant channels, respectively. Besides, the disdrometer can also provide rainfall quantities, including drop size distribution (DSD), reflectivity (Z, dBZ), rain rate (R_R, mm·h^{-1}) and rain amount (R_M, mm). The main technical parameters of these two instruments are listed in Table 2.

Table 2. The main technical parameters of ceilometer and disdrometer.

Ceilometer / Disdrometer	Items	Technical Specifications
Ceilometer	Sensor type	Laser, pulsed
	Wavelength	910±10 nm
	Peak power	27 W
	Sampling volume	834×266×264 mm^3
	Detection range	0-15 km
	Spatial resolution	10 m
	Temporal resolution	2 s
	Measurements	Backscatter profiles, cloud base height
Disdrometer	Sensor type	laser
	Peak power	≥2W
	Sampling height	1.4 m
	Sampling area	54 cm^2
	Measurable diameter range	0.062 – 24.5 mm
	Measurable velocity range	0.05 – 20.8 m s^{-1}
	Temporal resolution	60 s
	Measurements	Drop size distribution, reflectivity, rain rate, rain amount, weather code

2.2. Methods of data processing, quality control and physical quantity retrieval

Previous studies indicated that data quality issues can affect the application of Ka-band MMCR and laser disdrometer [57, 58]. Therefore, appropriate technologies of data processing and quality control (QC) are adopted in this study. Besides, specific retrieval methods are also used to obtain

Peer-reviewed version available at Remote Sens. 2019, 11, 3045; doi:10.3390/rs11243045

physical quantities concerned cloud-precipitation. Figure 2 shows a brief flowchart of data processing, QC, and cloud-precipitation physical quantity retrieval for MMCR and disdrometer we adopted. After processing, eventually, 18 kinds of instruments' measurements and retrievals are produced, including radar quality-controlled SP, Z, V_M, S_W, and LDR, new-calculated radar spectral skewness (S_K) and spectral kurtosis (K_T), and radar-derived (or disdrometer/ceilometer-measured) cloud-precipitation physical quantities of cloud base height (CBH, km), cloud top height (CTH, km), cloud thickness (CTK, km), cloud layer number (CLN), R_R, R_M, DSD, vertical air velocity (V_A, $m \cdot s^{-1}$), particle mean terminal velocity (V_T, $m \cdot s^{-1}$), particle mean diameter (D_M, mm), particle total number concentration (N_T, m^{-3}) and liquid water content (LWC, $g \cdot m^{-3}$). For convenience, abbreviations are used in this manuscript which can be found in the appendix (Table A). Each step in Figure 2 is explained in detail in the following subsections.

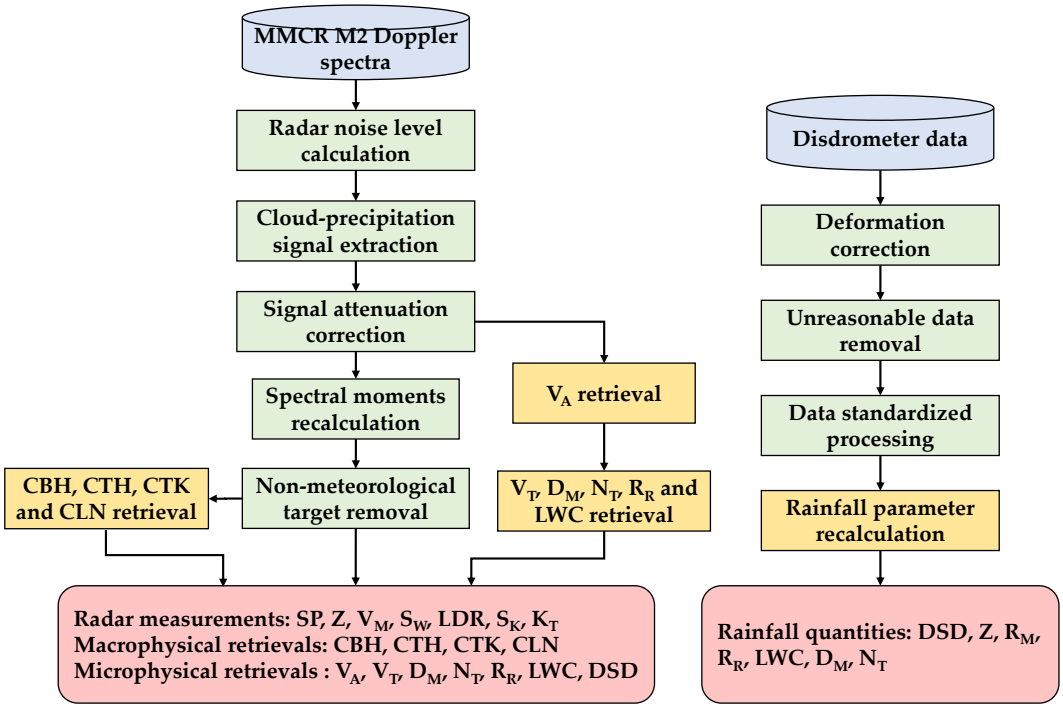

Figure 2. A flowchart of data processing, quality control and cloud-precipitation physical quantity retrieval for MMCR and disdrometer. The SP, Z, V_M, S_W, LDR, S_K, and K_T represent radar Doppler spectrum, reflectivity, mean Doppler velocity, spectrum width, linear depolarization ratio, spectral skewness, and spectral kurtosis, respectively; the CBH, CTH, CTK, and CLN denote radar-derived cloud base height, cloud top height, cloud thickness, and cloud layer number, respectively; the V_A, V_T, D_M, N_T, R_R, R_M, LWC , and DSD are vertical air velocity, particle mean falling velocity, particle mean diameter, particle total number concentration, rain rate, rain amount, liquid water content, and drop size distribution, respectively.

2.2.1. MMCR data processing, QC and physical quantity retrieval

The Ka-band MMCR undergoes attenuation as its electromagnetic wave passes through cloud-precipitation. Non-meteorological echo caused by plankton also contaminates radar data in the low-level atmosphere. Besides, the radar originally provides SP, Z, V_M, S_W and LDR, the other 12 kinds of measurements and retrievals remain to be further produced. Considering these, the following techniques were implemented.

(1) **Radar noise level calculation**. The cloud-precipitation signal is overlapped by radar noise in Doppler spectrum. For separation, an objective technology proposed by Hildebrand and Sekhon was utilized to estimate radar noise level [59].

(2) **Cloud-precipitation signal extraction.** All continuous spectral bins above radar noise level were picked out and further judged by a signal-to-noise ratio (SNR) threshold ($\geqslant$-12 dB) and a bin-

Peer-reviewed version available at Remote Sens. 2019, 11, 3045; doi:10.3390/rs11243045

number threshold (≥5), because cloud-precipitation signal typically has a higher power and larger spectral width than radar noise [57]. Only consecutive signals with the first two powers were reserved, as well as their SNRs, left endpoints, right endpoints, and peaks were also recorded.

(3) **Signal attenuation correction**. The radar returned signal is attenuated by hydrometeors, causing underestimations of the measured SP and Z. For correction, an iterative procedure was implemented [46, 57].

$$\mathrm{K}_i = \alpha Z_c(i)^{\beta} \quad (1)$$

$$\tau_i = \tau_{i-1} \times \exp(-2 \times K_i \times \Delta R) \quad (2)$$

$$\mathrm{Z_c(i)} = \frac{\mathrm{Z}_m(\mathrm{i})}{\tau_{\mathrm{i-1}}} \times \exp(K_i \times \Delta R) \quad (3)$$

$$\mathrm{SP}_c(n,i) = \frac{SP_m(n,i)}{\tau_{i-1}} \times \exp(K_i \times \Delta R) \quad (4)$$

In Equations (1-4), i and n denote the radar range gate number and spectral bin number, respectively, K_i (dB·km^{-1}) is the attenuation coefficient, τ_i is the radar wave two-way transmissivity, ΔR (30 m) is the gate length, Z_m and Z_c represent radar-measured and corrected reflectivity, respectively, SP_m and SP_c represent the radar-measured and corrected Doppler spectra, respectively. To start the iteration, the initial τ_0 and $Z_c(0)$ were set to 1 and $Z_m(0)$, respectively. The coefficients α and β were set to 0.00334 and 0.73, respectively [60].

(4) **Spectral moment recalculation**. After attenuation correction of SP, six radar moments including Z, LDR, V_M, S_W, S_K and K_T were recalculated by the following formulas,

$$\mathrm{P}_{c\&p} = \sum_{v=V_l}^{v=V_r} (SP_c(v) - P_N) \quad (5)$$

$$Z = 10 \times log_{10}\left(\frac{\mathrm{P}_{c\&p} \times R^2}{C}\right), C = \frac{P_t \times G^2 \times \theta \times \varphi \times h \times \pi^3 \times |k|^2}{1024 \times ln2 \times \lambda^2 \times L_\varepsilon} \quad (6)$$

$$LDR = Z_V - Z_H \quad (7)$$

$$V_M = \frac{\sum_{v=V_l}^{v=V_r} v \times (SP_c(v) - P_N)}{\sum_{v=V_l}^{v=V_r} (SP_c(v) - P_N)} \quad (8)$$

$$S_W = \left[\frac{\sum_{v=V_l}^{v=V_r} (v - V_M)^2 \times (SP_c(v) - P_N)}{\sum_{v=V_l}^{v=V_r} (SP_c(v) - P_N)}\right]^{1/2} \quad (9)$$

$$S_K = \frac{\sum_{v=V_l}^{v=V_r} (v - V_M)^3 \times (SP_c(v) - P_N)}{{S_W}^3 \times \sum_{v=V_l}^{v=V_r} (SP_c(v) - P_N)} \quad (10)$$

$$K_T = \frac{\sum_{v=V_l}^{v=V_r} (v - V_M)^4 \times (SP_c(v) - P_N)}{{S_W}^4 \times \sum_{v=V_l}^{v=V_r} (SP_c(v) - P_N)} - 3 \quad (11)$$

where, v denotes the Doppler velocity of spectral bin, V_l and V_r (m·s^{-1}) denote the left-endpoint and right-endpoint Doppler velocities of cloud-precipitation signal in spectra, respectively, $SP_c(n)$ (mW) is the signal power of each spectral bin, P_N (mW) is the noise level, $\mathrm{P}_{c\&p}$ (mW) represents total power of cloud-precipitation signal in spectra, R (km) is the distance from radar to target, C is the radar constant, P_t (W) is the radar transmitted power, G (dB) is the antenna gain, θ and φ (degree) are the radar horizontal and vertical beam widths, respectively, h (km) represents the spatial pulse length, λ (mm) for the radar wavelength, $|k|^2$ for the refractive index, L_ε (dB) is the feeder loss, Z_H and Z_V (dBZ) are two reflectivity received by radar parallel and cross-polarization channels.

(5) **Non-meteorological echo removal.** Non-meteorological echo in MMCR caused by low-level plankton, which consists of dust, insect, pollen, and other targets, were commonly observed in the low- and mid-latitude regions [61,62]. MMCR-measured Z can be used in conjunction with ceilometer-measured CBH to identify and remove the plankton echo [25]. However, this approach cannot get rid of the entire plankton echo, since partial of plankton actually exist above the CBH. Herein, we used a simple technology named "Z-LDR double-threshold" to eliminate the plankton contamination in MMCR data. This method is based on an observational fact that the Z and LDR distributions of plankton and warm cloud-precipitation are apparently different. Namely, the plankton echo can exhibit a very large LDR with a relatively small Z, in contrast, the warm cloud-

Peer-reviewed version available at Remote Sens. 2019, 11, 3045; doi:10.3390/rs11243045

precipitation echo generally owns a relatively small LDR with a wide range of Z. According to the realistic statistical result from MMCR data (as shown in Figure 3), the Z and LDR thresholds were simultaneously set to -8 dBZ and -14 dB, respectively. In this case, any radar range gate simultaneously owned a Z smaller than -8 dBZ and an LDR larger than -14 dB can be judged as plankton and then be removed. Under the action of "Z-LDR double-threshold", all plankton echo in LDR field can be fully filtered out as excepted, whereas, a part of scattered plankton will remain in other radar moments (Z, M_V, S_W, S_K, and K_T), which own a larger echo amount than LDR. Therefore, a 3×3 filtering window is further implemented to eliminate the remained scattered plankton [63].

(6) **Retrieval of cloud-precipitation macrophysical quantity.** The cloud-precipitation CBH, CTH, CTK, and CLN, were derived by using radar-measured Z. For each radar radial, continuous segments with more than 10 gates (300 m) of valid Z were distinguished and the segment base height and top height were taken as CBH and CTH, respectively. The segment number and length were regarded as CLN and CTK, respectively.

(7) **Retrieval of cloud-precipitation microphysical quantity.** Seven key microphysical quantities of warm cloud-precipitation, including V_A, V_T, D_M, N_T, R_R, LWC, and DSD were further deduced using processed radar Doppler spectra. First, a technology named "small-particle-traced" was applied to estimate V_A from Doppler spectra. This approach has been applied and verified by Gossard, Kollias, Shupe, Zheng, and Sokol in different cloud-precipitation studies [64-68]. The V_T was then obtained by subtracting V_A from V_M. Second, shifting the Doppler spectra according to V_A and converting the spectra unit from dBm to dBZ using Equation (5-6). A relationship between particle terminal velocity and diameter must be determined before further retrieval. For liquid hydrometeor, the used relationship can be written as [69,70],

$$D = \frac{1}{0.6} \times ln\frac{10.3}{9.65 - V_t/\delta(h)} \quad (12)$$

$$\delta(h) = 1 + 3.68 \times 10^{-5} h + 1.71 \times 10^{-9} h^2 \quad (13)$$

where D (mm) and V_t (mm·s^{-1}) denote the diameter and terminal velocity of the particle, h (m) is the radar sampling height above sea level, and $\delta(h)$ is a correction factor. Based on the above, radar-derived D_M, N_T, R_R, LWC, and DSD can be acquired by using the following formulas [46],

$$P_{D_i} = \frac{C \times D_i^6}{R^2} \quad (14)$$

$$N(D_i) = \frac{P_i}{P_{D_i} \times \Delta D_i} \quad (15)$$

$$D_M = \frac{\Sigma_{i=D_{min}}^{D_{max}} D_i \times N(D_i) \times \Delta D_i}{\Sigma_{i=D_{min}}^{D_{max}} N(D_i) \times \Delta D_i} \quad (16)$$

$$N_T = \sum_{i=D_{min}}^{D_{max}} N(D_i) \times \Delta D_i \quad (17)$$

$$R_R = \frac{6\pi}{10^4} \sum_{i=D_{min}}^{D_{max}} D_i^3 \times V_t(D_i) \times N(D_i) \times \Delta D_i \quad (18)$$

$$LWC = \frac{\pi}{6000} \sum_{i=D_{min}}^{D_{max}} \rho \times D_i^3 \times N(D_i) \times \Delta D_i \quad (19)$$

where ΔD_i (mm) is the diameter interval, P_{D_i} (mW) is the power caused by a single particle with a diameter of D_i, P_i (mW) is the radar-measured power for the particles with a diameter of D_i, D_{min} and D_{max} (mm) represent the detected minimum and maximum diameters in Doppler spectra, and ρ (g·cm^{-3}) is the water density.

2.2.2. Disdrometer data processing and QC

Parsivel disdrometer overestimates the size of a large non-spherical particle and suffers from bias under several unfavorable circumstances [51]. Therefore, to improve its data quality and recalculate rainfall quantities, the raw DSD was further post-processed as follows.

Peer-reviewed version available at Remote Sens. 2019, 11, 3045; doi:10.3390/rs11243045

(1) **Deformation correction.** The measured raindrop diameter which exceeds 1 mm will be overvalued because the disdrometer can measure only in the horizontal direction with an assumption that the passing hydrometeor is spherical. However, in nature, a large raindrop can distort to be ellipsoidal. Thus, a correction equation was utilized to correct the raindrop diameter [71],

$$D = \begin{cases} D_o & (D_o \le 1\ mm) \\ (1.075 - 0.075 \times D_o) \times D_o & (1\ mm < D_o \le 5\ mm) \\ 0.7 \times D_o & (D_o > 5\ mm) \end{cases} \quad (20)$$

where D_o (mm) is the original diameter and D (mm) represents the equivalent spherical diameter after correction.

(2) **Unreasonable data removal.** Three kinds of unreasonable data need to be removed from the dataset. First, removing any data with diameters greater than 6 mm, based on a fact that a raindrop will break up before growing up to 6 mm in the sea-level atmosphere. Second, any raindrop owns a normal falling velocity but with an excessively large or small diameter is treated as a problematic data, which can be produced when a large raindrop partially or multiple raindrops parallelly pass through the laser beam. Third, in contrast, any raindrop exhibits as a normal diameter but with an extremely large or small falling velocity is also regarded as an unrealistic data, which can be caused by strong wind shear or splashing from instrument surface during rainfall. The latter two kinds of unreasonable data were recognized by comparing the disdrometer-measured result with the theoretical V_T-D relationship shown in Equations (12-13). Any measured result outside ±60 % of the relationship was removed.

(3) **DSD standardization.** The DSD was further normalized by the following formula,

$$N(D_i) = \sum_{j=1}^{32} \frac{n_{ij}}{A \times \Delta t \times V_j \times \Delta D_i} \quad (21)$$

where D_i (mm) is the raindrop diameter for channel i; $N(D_i)$ ($\mathrm{m^{-3} \cdot mm^{-1}}$) is the number concentration of raindrop per unit volume with diameters in an interval from D_i to $D_i + \Delta D_i$, n_{ij} represents the raindrop number within size channel i and velocity channel j, A ($\mathrm{m^2}$) is the sampling area, and Δt (60 s) is the sampling time.

(4) **Rainfall quantity calculation.** Based on steps (1-3), six rainfall physical quantities, including Z, R_M, R_R, LWC, D_M and N_T, were recalculated using Equations (22-26).

$$Z = \sum_{i=1}^{32} \sum_{j=1}^{32} D_i^6 \times \frac{n_{ij}}{A \times \Delta t \times V_j} \quad (22)$$

$$R_R = \frac{R_M}{\Delta t} \times 3600 = \frac{6\pi}{10^4} \sum_{i=1}^{32} \sum_{j=1}^{32} D_i^3 \times \frac{n_{ij}}{A \times \Delta t} \quad (23)$$

$$LWC = \frac{\pi}{6000} \sum_{i=1}^{32} \sum_{j=1}^{32} \rho \times D_i^3 \times \frac{n_{ij}}{A \times \Delta t \times V_j} \quad (24)$$

$$D_M = \frac{\Sigma_{i=1}^{32} D_i^3 \times N(D_i) \times \Delta D_i}{\Sigma_{i=1}^{32} N(D_i) \times \Delta D_i} \quad (25)$$

$$N_T = \sum_{i=1}^{32} N(D_i) \times \Delta D_i \quad (26)$$

2.3. Warm cloud-precipitation determination

The whole dataset collected from April 15 to June 18 at the LM site were processed by the methods mentioned above, for our study purpose, only warm cloud-precipitation events were selected. A cloud-precipitation was determined as a warm event according to its MMCR-derived CTH, which should be lower than a height threshold of the zero-degree layer. According to the radiosondes, the zero-degree height of the atmosphere over the site was in a range from 4.2 km to 5.1 km during the observation period. Therefore, the height threshold was set to 4.2 km.

3. Results

Peer-reviewed version available at Remote Sens. 2019, 11, 3045; doi:10.3390/rs11243045

3.1. Data QC result

Plankton target occurs in the low-level of atmosphere and can affect the data usage of Ka-MMCR for cloud-precipitation observation. For separation of the plankton contamination from radar dataset, Z-LDR probability distributions of plankton and warm cloud-precipitation were respectively investigated. The statistic results were shown in Figure 3, and it indicates that the distributions of plankton and warm cloud-precipitation are obviously different in Z and LDR fields. Namely, the plankton owns a smaller Z mainly ranged from -41 to 1 dBZ with a remarkably large LDR within -22-18 dB. In contrast, the warm cloud-precipitation has a larger Z ranged from -9 to 38 dBZ with an apparently narrow scope of LDR from -29 to -22 dB. Based on these differences, a couple of thresholds for Z and LDR were set to -8 dBZ and -14 dB by preferentially considering that the warm cloud-precipitation should not be accidentally deleted. Verification demonstrates that 92.22% of the entire plankton targets can be removed from the Ka-MMCR dataset using this Z-LDR threshold combined with a 3×3 filtering window, meanwhile, the warm cloud-precipitation echo remains well. Form another view, Figure 4 shows the cumulative probability of Z and LDR of the radar dataset before and after QC. By comparing the LDR and Z curves, we can find that the LDR mainly distributes within -27-15 dB before QC, whereas, it concentrates in a range from -27 to -11 dB and the probability of Z lower than -1 dB is decreased after QC, as a result of plankton elimination. Besides, the result shows the probability of Z from 0 to 27 dBZ is increased after QC because of attenuation correction.

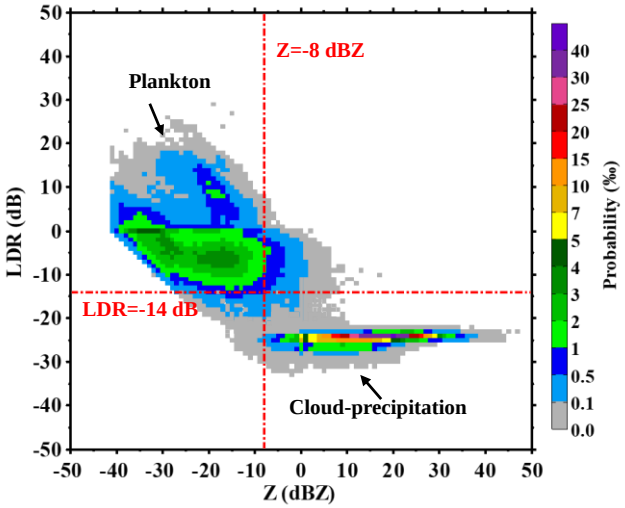

Figure 3. Ka-MMCR reflectivity-linear depolarization ratio (Z-LDR) probability distributions of warm cloud-precipitation and plankton. A couple of Z and LDR thresholds are set to -8 dBZ and -14 dB to eliminate the plankton.

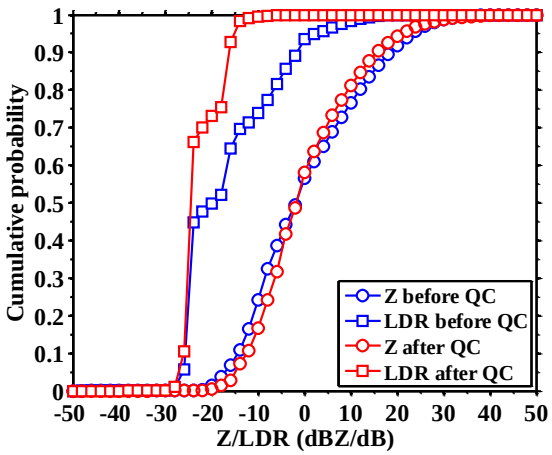

Figure 4. Cumulative probability curves of Ka-MMCR reflectivity (Z) and linear depolarization ratio (LDR) before and after data quality control (QC).

Peer-reviewed version available at Remote Sens. 2019, 11, 3045; doi:10.3390/rs11243045

In order to present the impact of the radar QC, a typical case that contains different types of warm cloud-precipitation and plankton is plotted in Figure 5. It can be seen that there exist warm convections, several cumuli, and layers of fracto-cumulus successively passed over the site in the low-level atmosphere during the observation period. The warm convection (1200-1330 BJT) has a relatively large scale and a high CTH and was hardly surrounded by plankton, because of the influences of rain wash and downdraft. The hydrometeors in convection contribute to radar-measured LDR with a small value range from -26 to -24 dB [Figure 5(c)]. Whereas, after 1330, scattered plankton targets gradually appear around the small-scale cumuli and fracto-cumuli. The plankton targets mainly located under 1.5 km with an extremely large LDR greater than -14 dB. From Figure 5(c-d), it can be clearly seen that the scattered plankton targets are well eliminated (as marked by the arrows) after QC, meanwhile, the small-scale cloud-precipitation such as the weak cumuli and thin fracto-cumuli during 1800-2000 remains unchanged. Deviation of Z before and after QC as shown in Figure 5(e) illustrates that most Z of cloud-precipitation suffers from small attenuation with a value lower than 0.1 dB. However, for stronger and thicker precipitating cumuli and convection (as marked by the circles), the Z attenuation can be slightly larger than the other clouds with a value within 0.2-0.4 dB under the cloud top.

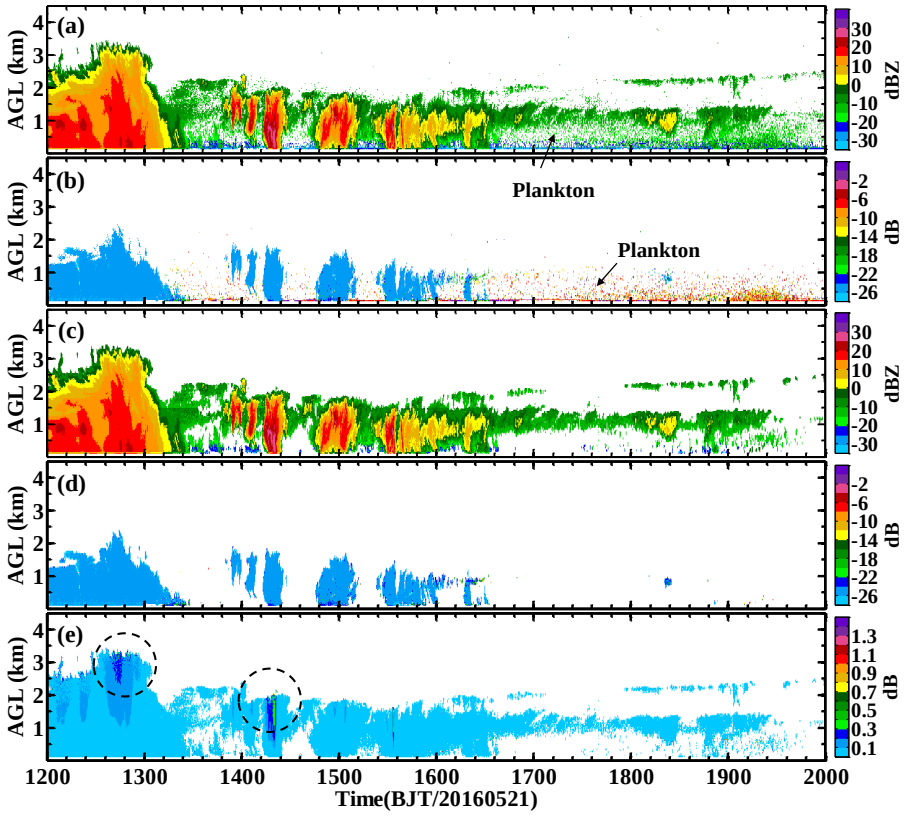

Figure 5. Time-height cross sections of original reflectivity (a), original linear depolarization ratio (b), reflectivity after QC (c), linear depolarization ratio after QC (d), and the deviation (e) between (a) and (c), observed by Ka-MMCR on May 21, 2016.

To illustrate the QC effect of disdrometer, the measured diameter (D) and falling velocity (V_f) of raindrops in different channels were counted. Figure 6 shows the D-V_f frequency distributions before and after QC. Comparing their differences, it is seen that the distribution of raindrops with a diameter greater than 1 mm has been corrected, exhibiting a slightly left shift along the diameter coordinate. A part of raindrops, which own a normal D/V_f with an unrealistic V_f/D and distribute far away from the theoretical curve, are eliminated after QC. In addition, any large raindrops greater than 6mm, which actually will break up under sea level pressure of the atmosphere, were also removed. Statistical results in Figure 6 also indicates that the disdrometer-measured V_f of raindrops is mostly greater than the result of the theoretical relationship because

Peer-reviewed version available at Remote Sens. 2019, 11, 3045; doi:10.3390/rs11243045

the latter is inferred under a still air condition, whereas, the former is actually overlapped by air downdraft. To further evaluate the QC effect, Figure 7 presents frequencies of raindrops in different D and V_f before and after QC, comparisons declare that a large part of small raindrops with D less than 0.312 mm related to unrealistic V_f were excluded, as well as some large raindrops with D greater than 2.75 mm were also regarded as unreliable measurements. For V_f, a large part of small raindrops with V_f less than 1 m/s and a small part of large raindrops with V_f greater than 15.1 m/s were both taken as problematic data under abnormal circumstances as detailedly described in subsection 2.2.2. Totally, 19.41 % of the entire DSD of the disdrometer is removed after QC.

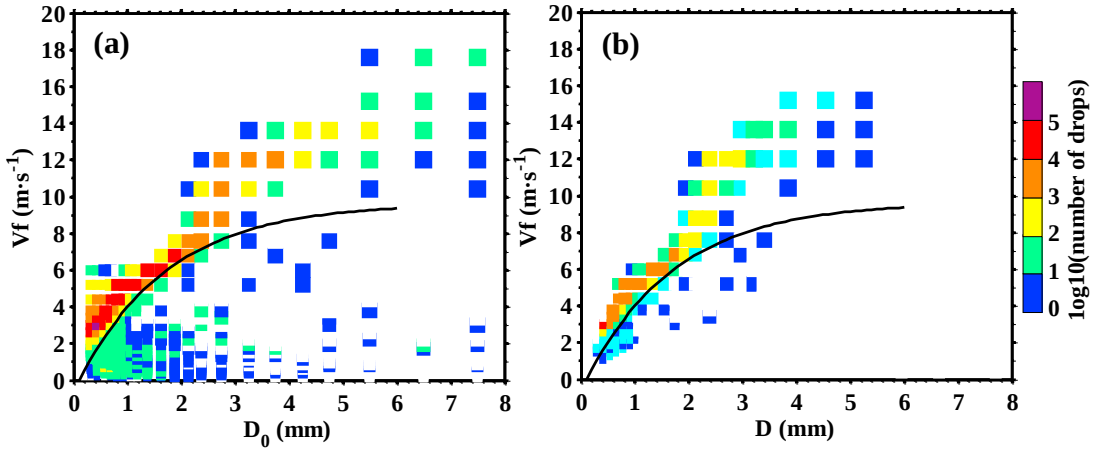

Figure 6. Raindrop diameter (D) -falling velocity (V_f) frequency distributions before (a) and after QC (b) for the entire disdrometer dataset. D_0 represents the raw raindrop diameter, D represents the corrected raindrop diameter, V_f is the raindrop falling velocity, the solid line represents the D-V_f theoretical relationship under a still air condition.

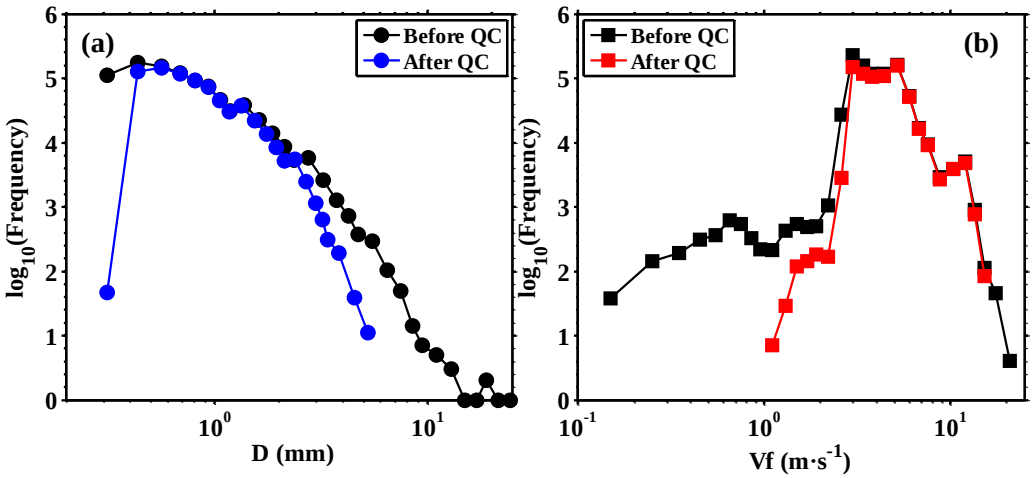

Figure 7. Frequencies of raindrops in different diameter (D) channels (a) and falling velocity (V_f) channels (b) before and after QC.

3.2. General characteristics of hydrometeor distribution

The QC dataset of Ka-MMCR and disdrometer was used to investigate the general characteristics of hydrometeor distribution over and on the LM site during the observation period. Figure 8(a) presents a statistical result of radar observation rates at different height levels (defined as the ratio of radial number with valid cloud-precipitation echo to the total radial number at each range gate). It shows that the majority of warm cloud-precipitation lies in the low-level atmosphere under 4.2 km with radar observation rates gradually increase as altitude decreases. 78.78% of the entire hydrometeors are concentrated below 2 km. Radar observation rates basically tend to be stable within

Peer-reviewed version available at Remote Sens. 2019, 11, 3045; doi:10.3390/rs11243045

0.84-0.39 km; subsequently, they continue to increase to a maximum of 12.4 % at 0.21 km. Figure 8(b) presents disdrometer-measured accumulated rain duration and rain amount under five R_R regimes (0-0.1 mm·h^{-1}, 0.1-1 mm·h^{-1}, 1-5 mm·h^{-1}, 5-10 mm·h^{-1}, >10 mm·h^{-1}). The result reveals that the ground rainfall is dominated by light precipitation most of the time, with 77.64 % of the entire duration owns an R_R smaller than 1 mm·h^{-1}. This part of rainfall is produced by weak cumulus and stratocumulus. 22.36 % of the entire duration has an R_R greater than 1 mm·h^{-1}, and they can be contributed by strong cumulus and convection. Despite a large contribution in time, light precipitation with a R_R smaller than 1 mm·h^{-1} only occupies 10.08 % of the total rain amount, in contrast, the stronger precipitation with an R_R greater than 1 mm·h^{-1} produces 89.92 % of the total rain amount. Especially under an R_R greater than 10 mm·h^{-1}, 3.58 % of the rain duration can induce 52.75 % of the entire rain amount, which corresponding to short-time strong showers. In detail, contributions to the entire rain duration and rain amount under five R_R regimes are (40.88%, 36.76%, 15.76%, 3.02%, and 3.58%) and (1%, 9.08%, 23.12%, 14.05%, and 52.75%), respectively.

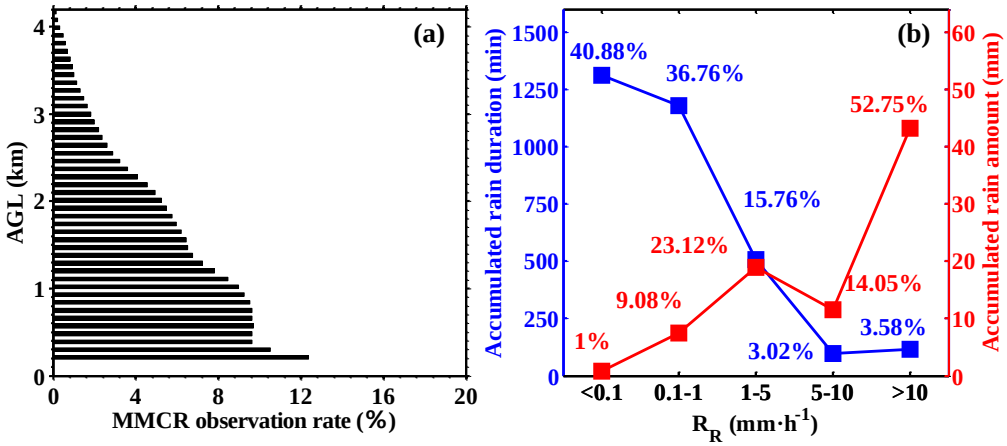

Figure 8. Ka-MMCR observation rates of warm cloud-precipitation at different height levels (a) and disdrometer-measured accumulated rain duration and rain amount under five rain rate (R_R) regimes (b).

3.3. Diurnal variation of warm cloud-precipitation

The 18 kinds of measurements and retrievals of the three instruments were further utilized to synthetically elucidate the diurnal variation of warm cloud-precipitation events that happened during the pre-flood season over the LM site.

Firstly, the diurnal time series of three macrophysical quantities, including CBH, CTH, and CTK, were investigated as shown in Figure 9. The statistics of ceilometer-measured results [Figure 9(a)] show that warm cloud-precipitation owns an average CBH ranging from 0.95 to 1.6 km. Despite exhibiting a quite low cloud base, a gradually rising trend of CBH during 1200-2300 can be found attributed to the intensification of solar radiation. Comparing the ceilometer-measured CBH with the MMCR-derived counterpart, the latter is perceived to be basically reliable with a similar variation trend and a bias approximately within 0.5 km. Whereas, the MMCR-derived CBH is more fluctuant due to the limitations of radar sensitivity and precipitation effect. For weak cloud layers, MMCR overestimates the CBH to some extent, because the radar sensitivity (the minimum detectable reflectivity of radar precipitation mode at 1km is -32.1 dBZ) is limited to observe some very small particles near cloud base, such as the results during 1500-1700. For another case, under precipitating condition, MMCR can underestimate the CBH, because it takes the echo base as the CBH, such as the results from 1800 to 2100. Overall, the CBH during 1200-2300 is approximately 0-0.5 km higher than other times. Figure 9(b-c) present the MMCR-derived CTH and CTK; they reveal that warm cloud-precipitation is shallow with an average CTH from 1.2 to 2.25 km and an average CTK from 0.5 to 1.6 km. The CTH and CTK also frequently fluctuate in time series and exhibit a generally increase during 1200-1900 in the afternoon. At other times, there exist some periods with higher but discontinuous

Peer-reviewed version available at Remote Sens. 2019, 11, 3045; doi:10.3390/rs11243045

CTH and CTK, such as during 0300-1030 and 2100-2230.

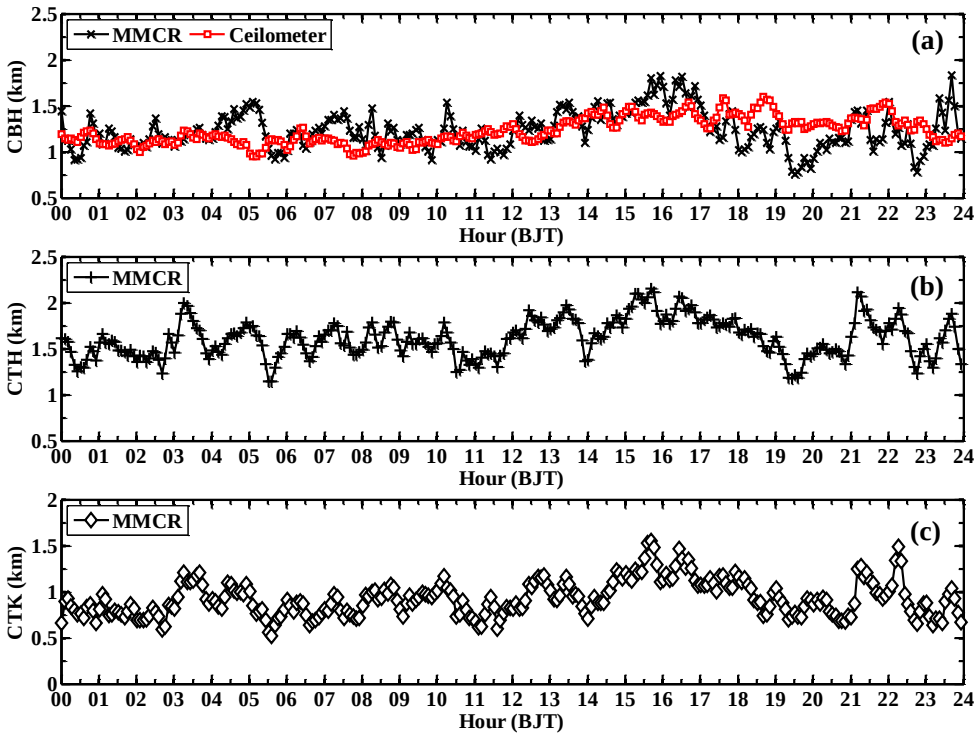

Figure 9. Diurnal time series of cloud base height (CBH) (a), cloud top height (CTH) (b), and cloud thickness (CTK) (c) measured by MMCR and ceilometer during observation period.

Secondly, MMCR spectral moments and microphysical retrievals are counted to form mean time-height results to analyze the diurnal variation of aloft cloud-precipitation properties. Figure 10 the diurnal statistics of the MMCR-measured Z, V_M, S_W, S_K, and K_T. The Z image [Figure 9(a)] indicates that most of the warm cloud-precipitation is lower than 3 km; however, a small part can approach to 3.5-4 km. The relatively strong echo mainly concentrates on three periods, namely, 0230-1100, 1200-1800, and 2100-2300, which is a similar feature with the result from Figure 9. During these three periods, the Z discontinuously fluctuates, and its value can reach up to 5-20 dBZ, which corresponding to higher cloud tops and attributed to short-time convections. The convections actually occupy a small proportion of the entire cloud-precipitation events and are the most frequent during 1200-1800 as a result of the solar radiation heating effect. At other times, the Z is relatively weaker in a range from -10 to 0 dBZ, with lower cloud tops and fewer convections. Radar-measured V_M [Figure 10(b)] is all negative, implying the updraft is weak in the cloud body; radar Doppler velocity is basically dominated by downdraft and particle terminal velocity. Radar-measured S_W [Figure 10(c)] exhibits relatively high values exceeding 0.75 $m \cdot s^{-1}$ to the convections, especially in the middle and upper part of the cloud body, suggesting cloud droplet growth in this area. The S_k [Figure 10(c)] is small within -0.4-0.4 for the entire time-height image, indicating that physical processes in warm cloud-precipitation are temperate, which can lead to forming symmetrical hydrometeor signal in radar spectra. However, the K_T shows a difference between the cloud middle-upper part and lower part, that is the cloud middle-upper part mostly has a negative K_T reflecting mild cloud droplet growth process to form obtuse radar spectra, in contrast, the lower part of cloud owns a positive K_T due to raindrop rapid collision and coalescence processes to produce peaky radar spectra.

Peer-reviewed version available at Remote Sens. 2019, 11, 3045; doi:10.3390/rs11243045

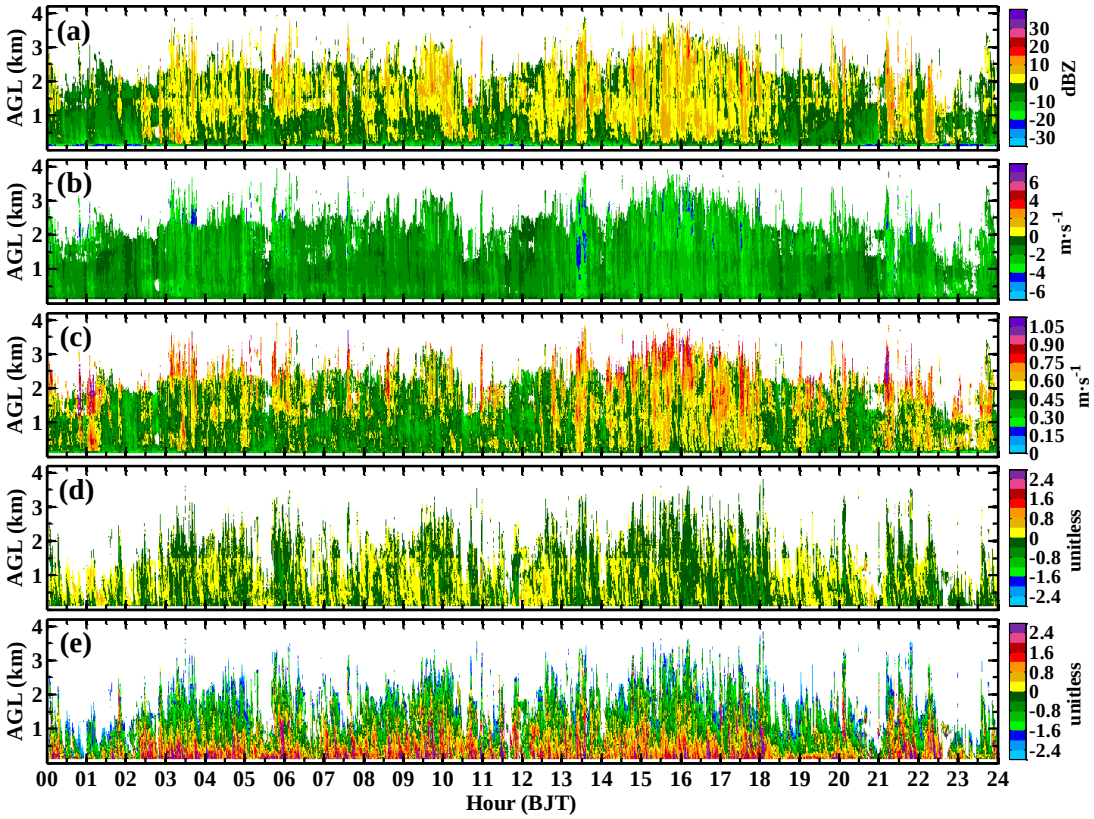

Figure 10. Diurnal time-height statistics of MMCR five spectral moments, reflectivity Z(dBZ) (a), mean Doppler velocity V_M ($m \cdot s^{-1}$) (b), spectrum width S_W ($m \cdot s^{-1}$) (c), spectral skewness S_K (unitless) (d), and spectral kurtosis K_T (unitless) (e).

For directly characterizing the diurnal variation of cloud-precipitation microphysical properties. Figure 11 presents diurnal time-height statistics of MMCR-retrieved V_T, V_A, D_M, N_T, LWC, and R_M. Figure 11(a) shows that the particle mean terminal velocity V_T is generally small within -3-0 $m \cdot s^{-1}$. In relative terms, the V_T is larger during the three periods than other times, relating to convections which own larger particles. Comparing V_A results in Figure 11(b-d), it is found that the vertical air motions in the warm cloud-precipitation are very weak. The downdraft (the negative V_A) and the updraft (the positive V_A) are within -3-0 $m \cdot s^{-1}$ and 0-3 $m \cdot s^{-1}$, respectively. The downdraft mainly distributes throughout the entire cloud-precipitation, especially for some convections, the larger downdraft even concentrates in the mid- and upper part of the cloud body. However, the updraft mainly located in the lower part of the cloud-precipitation, only for few individual convections, the updraft can be larger than 2-3 m/s. The D_M and N_T [Figure 11(e-f)] results illustrate that the mean diameter and number concentration of warm cloud-precipitation are in ranges from 0.1 to 0.5 mm and from 10^2 to 10^5 m^{-3}. The larger particles consist of raindrops are mostly distributed under CBH with diameters from 0.25 to 0.5 mm and number concentrations from 10^2 to 3.16×10^3 m^{-3}. In contrast, above the CBH, the cloud droplets are relatively small and mostly own diameters from 0.1 to 0.25 mm and number concentrations from 3.16×10^3 to 10^5 m^{-3}. The derived LWC and R_R images [Figure 11(e-h)] demonstrate that the warm cloud-precipitation averagely own liquid water content and rain rate in ranges from 0 to 0.5 $g \cdot m^{-3}$ and 0 to 3 $mm \cdot h^{-1}$, respectively. During the three periods (0230-1100, 1200-1800, and 2100-2300), the frequent convections own relatively large liquid water and produce relatively stronger rainfall, whereas, at other times, the LWC and R_R are very limited. Overall, the derived LWC and R_R present coherent features as the counterparts of Z and V_T, which can imply that the warm cloud-precipitation events have more water content and stronger rainfall during the three periods.

Peer-reviewed version available at Remote Sens. 2019, 11, 3045; doi:10.3390/rs11243045

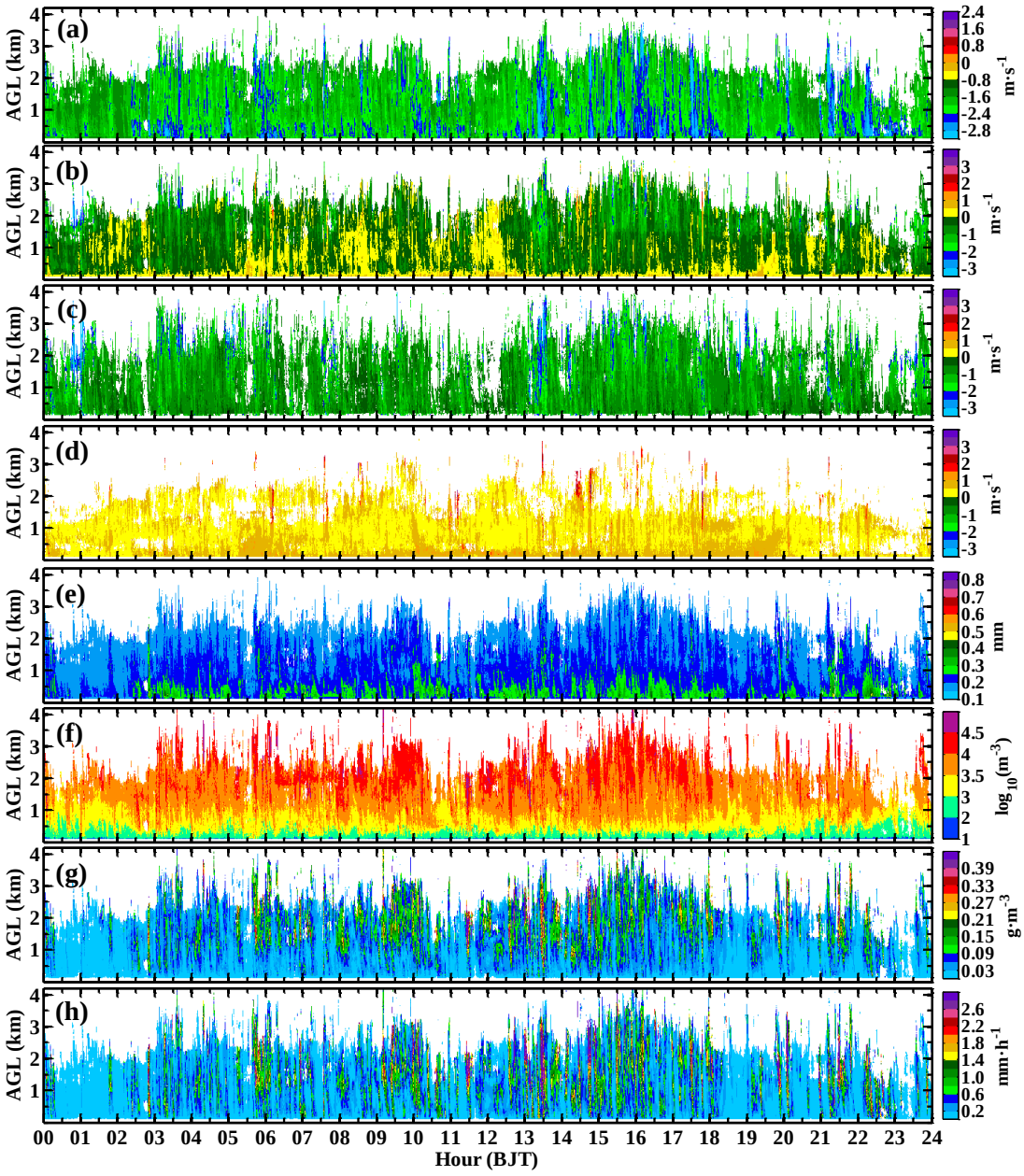

Figure 11. Diurnal time-height statistics of MMCR retrievals, particle mean terminal velocity V_T ($m \cdot s^{-1}$) (a), vertical air velocity V_A ($m \cdot s^{-1}$) (b), downdraft velocity (negative V_A) (c), updraft velocity (positive V_A) (d), particle mean diameter D_M (mm) (e), particle total number concentration N_T (m^{-3}) (f), liquid water content LWC ($g \cdot m^{-3}$) (g), and rain rate R_M ($mm \cdot h^{-1}$) (h).

The ground-measured rainfall quantities obtained by disdrometer were also calculated to complement the radar observations. Figure 12 shows the diurnal cycles of ground rainfall occurrence, diameter channel occurrence, Z, D_M, N_T, R_R, R_M, and LWC. Herein, the rainfall occurrence is defined as the ratio of the rainy minute number to the total operation minute number, and the diameter channel occurrence is defined as the ratio of the minute number of each diameter channel with valid raindrops to the total operation minute number. These two variables can reflect the occurrence of rainfall events in the time domain and contributions of different diameter channels, respectively. Figure 12 (a-b) indicates that the rainfall frequently occurs during the same three periods as MMCR, the rainfall occurrences gradually reach up to peaks of 9.21%, 9.2%, and 6.58% at moments of 0427, 1550, and 2200 during these periods. The rainfall occurrence mostly represented by small raindrops with diameter channels within 1.06 mm. The mean DSD image [Figure 12(c)] proposes that the raindrops are inhomogeneous at different moments with apparent variations of their diameters and

Peer-reviewed version available at Remote Sens. 2019, 11, 3045; doi:10.3390/rs11243045

number concentrations, implying multiple types of warm cloud-precipitation both contribute to the ground rainfall. The raindrops of warm precipitation are quite small and sparse, with most of their diameters smaller than 1.75 mm and number concentrations from 10^2 to 10^4 $m^{-3}\cdot mm^{-1}$. Only a small part of raindrops can reach up to 1.75-3.85 mm but with a limited number of concentrations of lower than 10^2 $m^{-3}\cdot mm^{-1}$. The mean Z [Figure 12(d)] irregularly distributes in a range from -10 to 30 dBZ with an inconspicuous diurnal variation trend. The mean N_T and D_M of raindrops [Figure 12(e-f)] are mostly less than 10^3 m^{-3} and in a range from 0.5 to 1.5 mm, respectively. The mean R_R, R_M, and LWC [Figure 12(g-i)] have great variations in ranges from ~0 to 34.4 $mm\cdot h^{-1}$, from ~0 to 1.61 mm, and from ~0 to 1.21 $g\cdot m^{-3}$, respectively. They both exhibit several peaks during the three periods, at which their values are much larger than their counterparts at other moments as a result of more frequent convections. Theoretically, Z, R_R, and LWC are proportional to the 6th/3rd/3rd power of particle diameter and the 1st/1st/1st power of particle number concentration, respectively. Therefore, to further view the contributions of particle size and number concentration to rainfall quantities, herein, two groups of correlation coefficients (CCs) of D_M-Z, D_M-R_R, and D_M-LWC (group 1), and N_T-Z, N_T-R_R, and N_T-LWC (group 2) are calculated, respectively. In general, a CC can represent the variation trend of two variables; specifically, herein, it can also imply either particle size or number concentration of raindrops dominate the Z/ R_R/LWC. The CCs of two groups are 0. 8169, 0. 67, and 0.6815 (group 1), and 0.6266, 0. 4777, and 0.5844 (group 2), respectively. They conclude that the rainfall Z is mostly dominated by raindrop diameter, as usual. However, R_R and LWC are not greatly dominated by particle diameter, but also with quite apparent contributions of particle number concentration. In addition, the CC of R_R and R_M is 0.8544, which indicates the rain amount of warm precipitation is not induced by rainfall duration but produced by strong showers with large R_R. This find is agreed with the result of Figure 8(b).

Peer-reviewed version available at Remote Sens. 2019, 11, 3045; doi:10.3390/rs11243045

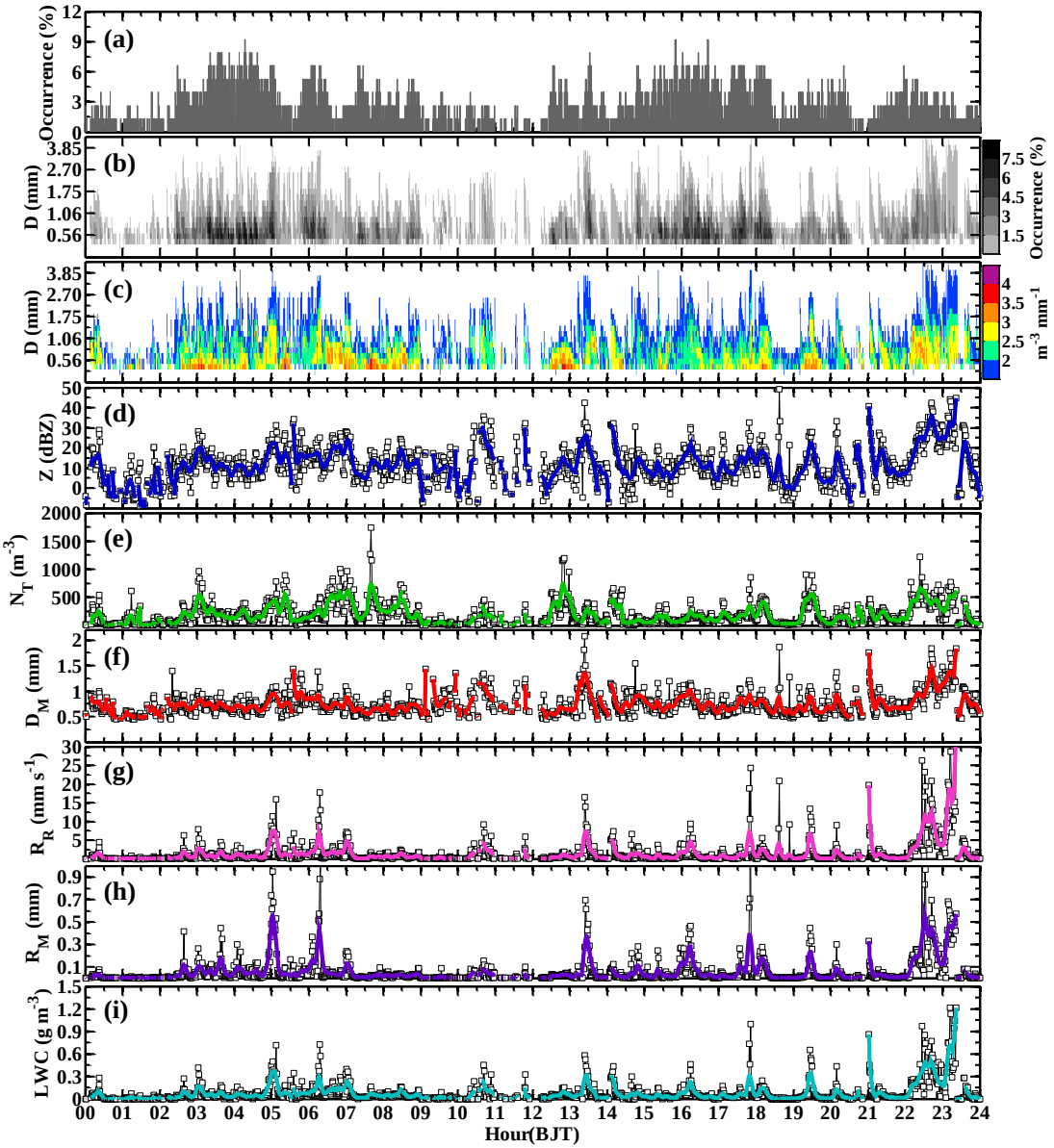

Figure 12. Diurnal variations of ground rainfall occurrence (a), raindrop diameter occurrence (b), raindrop size distribution (c), reflectivity Z(dBZ) (d), particle mean diameter D_M(mm) (e), total number concentration N_T(m^{-3}) (f), rain rate R_R ($mm \cdot s^{-1}$) (g), rain amount R_M (mm) (h) , and liquid water content LWC ($g \cdot m^{-3}$) (i) measured by ground disdrometer.

3.4. Vertical structures of warm cloud and precipitation

The vertical structure reflects the thermodynamic and microphysical processes in cloud-precipitation. Although basic results of vertical structures of warm cloud-precipitation have been described in subsection 3.3, clearer features and differences between cloud and precipitation are further studied in this subsection. Figure 13 shows the occurrences of CBH, CTH, CTK, and CLN at different height levels measured by the ceilometer and MMCR. The ceilometer-measured results [Figure 13(a)] indicate that the CBH of warm cloud-precipitation is in a range from 0.3 to 4 km, and the occurrence rapidly increases along with height between 0.3 and 0.9 km to reach up to a maximum of 8.47%. Whereas, after that, the occurrence gradually decreases as height increases. Most of the CBH with an accumulated occurrence of 90.23% is below 2.2 km. The CTH presented in Figure 13(b) demonstrates that the MMCR-measured CTH is relatively decentralized and distributes in a range from 0.6 to 4.2 km. The CTH occurrences at different heights both seem to be nonnegligible with values from 1% to 5% as a result of the certain existence of various types of cloud-precipitation over

Peer-reviewed version available at Remote Sens. 2019, 11, 3045; doi:10.3390/rs11243045

the observation site. Considering the advantages and disadvantages of the MMCR and ceilometer, the CTK is a synthetic result obtained by subtracting the ceilometer-measured CBH from the MMCR-measured CTH. The result [Figure 13(c)] presents a similar variation trend as the CBH with a value range from 0.15 to 3.6 km. A majority of CTK with 91.72% is thinner than 2.1 km, and a maximum of 13.8% is located at 0.6 km. For the cloud layer number, Figure 13(d) proposes that 76.1% of CLN is single, the occurrences of two-layer and three-layer CLN are 20.6% and 3.29%, respectively.

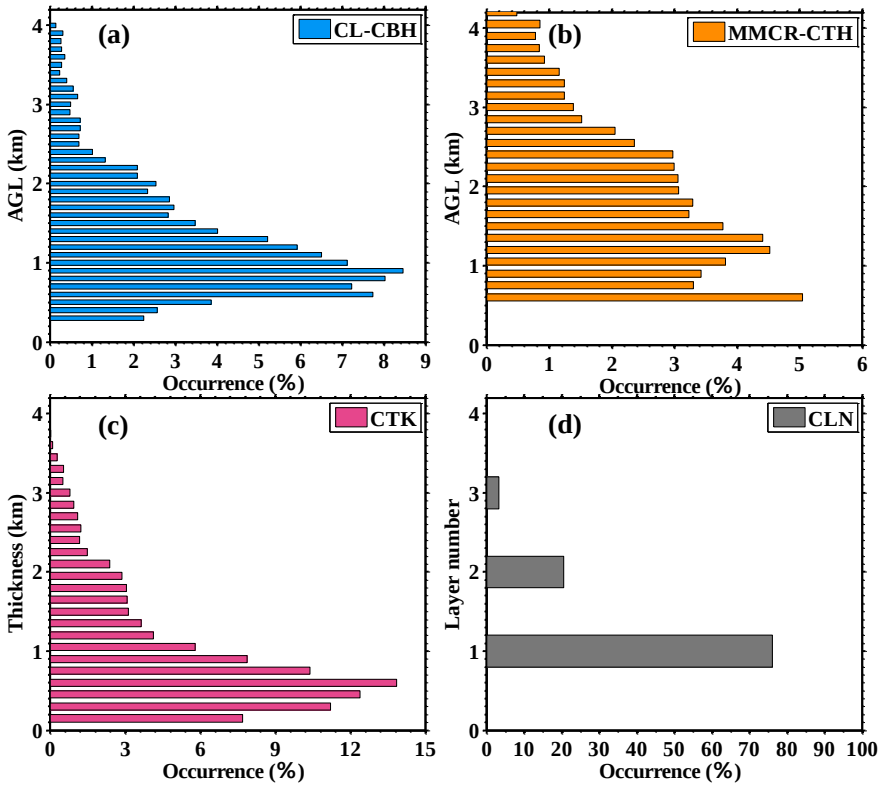

Figure 13. Occurrences of ceilometer-measured cloud base height CBH (a), MMCR-derived cloud top height CTH (b), synthetic cloud thickness CTK (c), and cloud layer number CLN (d).

Cloud and precipitation own different hydrometeors and experience different physical processes. Therefore, to investigate their features and differences in the vertical orientation, the MMCR measurements and retrievals were further divided into two groups, that is a group for cloud and another group for precipitation. The division is based on the ceilometer-measured CBH; namely, the MMCR result at any range gate is determined as a cloud target when it locates above the CBH, oppositely, it was taken as a precipitation target when it lies under the CBH. Furthermore, for convenient analysis of the vertical structures of cloud and precipitation, herein, the normalized contoured frequency by attitudes diagrams (NCFADs), which is a kind of diagram typically used to show the occurrence frequency distribution of radar measurements at each height level, are calculated and analyzed.

Figure 14 presents the NCFADs of MMCR five measurements, including Z, M_V, S_W, S_K, and K_T. Comparing the results between cloud and precipitation, as shown in Figure 14(a1-e1) and (a2-e2), respectively, several conclusions can be addressed as follows: (I) these measurements of cloud and precipitation have certain differences of frequency distributions in the height and value ranges. (II) Their height ranges of cloud mostly distribute within 0.3-4.2 km. However, the counterparts of precipitation located at lower height levels approximately below 2.3 km. (III) For convenience, occurrences greater than 0.3 ‰ are used to represent the majority distribution of the five measurements. In this case, for Z [Figure 14(a1) and (a2)], it can be seen that the cloud reflectivity is in a narrower range from -15 to 10 dBZ within 0.57-2.55 km, in contrast, the precipitation reflectivity is in a broader range from -22 to 24 dBZ with lower height levels below 1.26 km. The reflectivity

Peer-reviewed version available at Remote Sens. 2019, 11, 3045; doi:10.3390/rs11243045

frequency centers of cloud and precipitation appear at (1km, -10 dBZ) and (0.51km, -14 dBZ), respectively, and most of the precipitation is stronger than the cloud despite a part of weaker targets attributed to fogs, water vapor, and turbulence. (IV) The M_V of cloud and precipitation mostly distribute within 0-4 m/s and 0-6.4 m/s, respectively, indicating the precipitation consisted of raindrops owns larger terminal falling velocity than the cloud, which composed of cloud droplets. The cloud and precipitation have comparable S_W with ranges from 0 to 0.9 $m \cdot s^{-1}$ and 0 to 1.05 $m \cdot s^{-1}$, respectively. The M_V and S_W of precipitation decrease more rapidly than the cloud counterparts as heights declines, implying the collision and coalescence processes of raindrops are remarkable within a falling path near 2 km and the cloud particle growth with formation of large cloud droplets mainly occurs in the middle part of cloud body. (V) The cloud particle spectrum changes more moderately than the precipitation along with height, with majorities of S_K and K_T concentrate within -0.6-0.4 and -2.4-2, whereas, S_K and K_T of the latter are relatively unconcentrated and distributed in ranges from -2 to 1.2 and from -2.4 to 6, respectively. These differences denote that the small and large cloud droplets contribute to comparable radar signals corresponding to relatively symmetrical and flat radar Doppler spectra. In contrast, the raindrop changes more complicatedly, relating to both the small-raindrop dominated DSD and the large-raindrop dominated DSD can be both appeared under different circumstances. Besides, the ranges of S_K and K_T of cloud and precipitation both increase as height decrease, suggesting the particle spectrum both become wider as a result of cloud particle growth and raindrop collision/coalescence.

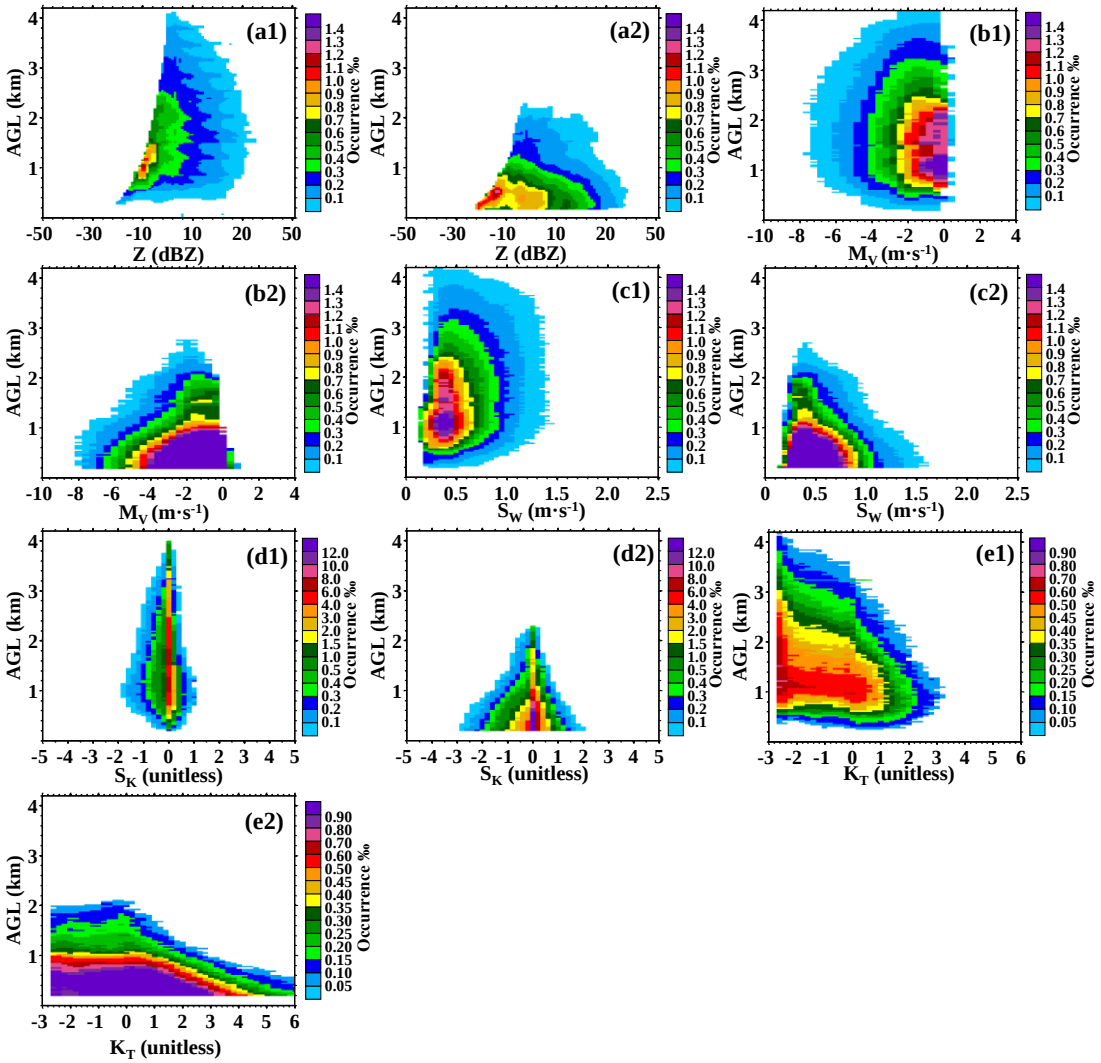

Figure 14. Normalized frequency by altitude diagrams (NCFADs) of Ka-MMCR measurements. (a1-e1) are radar reflectivity Z, mean Doppler velocity M_V, spectrum width S_W, spectral skewness S_K, and spectral kurtosis K_T, respectively, for cloud. (a2-e2) are the same quantities as (a1-e1), but for

Peer-reviewed version available at Remote Sens. 2019, 11, 3045; doi:10.3390/rs11243045

630 precipitation.

631 The NCFADs of MMCR-derived V_T, V_A, D_M, N_T, LWC, and R_R are further shown in Figure 15 (a1-
632 f1) and (a2-f2) to compare the features and differences of dynamic and microphysical properties of
633 cloud and precipitation. Comparisons of the six retrievals reveal that: (I) these retrievals of cloud and
634 precipitation concentrate in different value and height ranges with a similar feature as found in
635 Figure 14. (II) For clearer comparison, occurrences higher than the 3rd tick in color bar of the NCFADs
636 are used to represent the majority distributions of the retrievals. In this case, it can be seen that the
637 cloud droplets own much slower terminal falling velocities than the precipitation raindrops due to
638 smaller sizes. The V_T of cloud droplets and raindrops are in ranges from -1.8 to 0 $m \cdot s^{-1}$ and from -4.2
639 to 0 $m \cdot s^{-1}$, respectively. The V_T of raindrops in precipitation rapidly decrease along with height as a
640 result of collision and coalescence effects, whereas, the V_T of cloud droplets decreases much slowly
641 and conversely turns to increase near the cloud base due to evaporation effect. (III) Despite the vertical
642 air motions are both small in the interior of cloud and precipitation, the updraft and downdraft in
643 the latter are stronger than that in the former. Their V_As are in ranges from -1.4 to 1.2 $m \cdot s^{-1}$ and from
644 -0.8 to 0.6 $m \cdot s^{-1}$, respectively. The updraft and downdraft in precipitation both increase as height
645 decreases, the updraft mainly occurs in the low level and gradually weakened by the rainfall scour,
646 and the downdraft increase mainly attributed to the rainfall drag and evaporation effects. (IV) The
647 precipitation has much larger hydrometeor than the cloud, their D_Ms are in ranges from 0.18 to 0.48
648 mm and from 0.152 to 0.216 mm, respectively. Oppositely, the cloud owns more particle number than
649 the precipitation, their N_Ts are in ranges from 6.3×10^2 to 2×10^4 m^{-3} and from 6.3×10^1 to 3.98×10^3 m^{-3},
650 respectively. The droplets in the cloud middle part can be slightly larger than that in the cloud lower
651 and upper part because of the particle growth process. The larger raindrops gradually yield as height
652 decreases attributed to the collision and coalescence processes. The particle numbers of cloud and
653 precipitation are both gradually decrease along with height. (V) The cloud and precipitation both
654 own comparable LWCs with values range from 0 to 0.45 $g \cdot m^{-3}$ and from 0 to 0.5 $g \cdot m^{-3}$, respectively.
655 Due to the larger terminal falling velocity, the precipitation has relatively a larger R_R than the cloud,
656 their values range from 0 to 1.4 $mm \cdot h^{-1}$ and from 0 to 2.2 $mm \cdot h^{-1}$, respectively.

Peer-reviewed version available at Remote Sens. 2019, 11, 3045; doi:10.3390/rs11243045

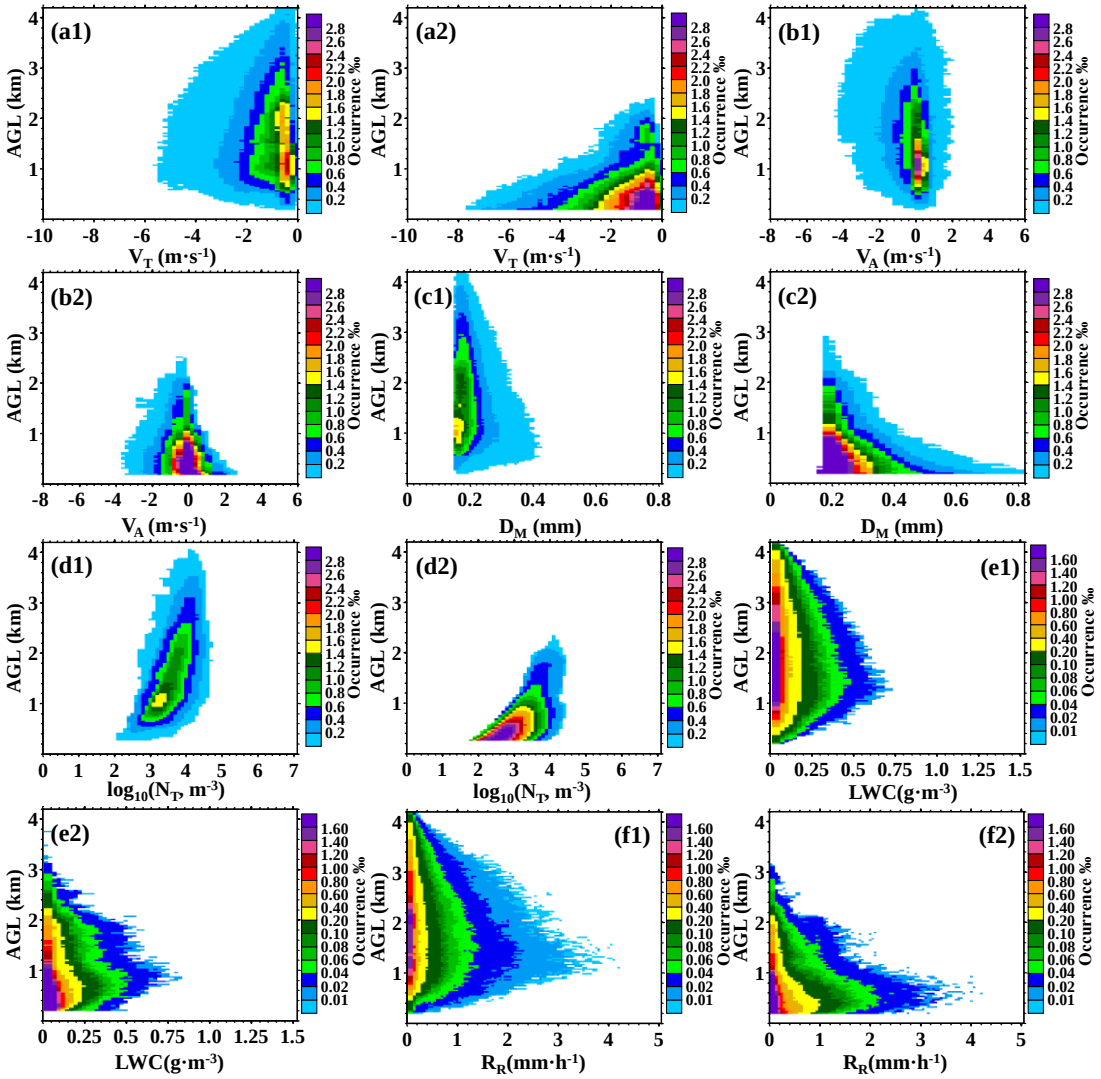

Figure 15. Normalized frequency by altitude diagrams (NCFADs) of Ka-MMCR retrievals. (a1-f1) are particle mean terminal velocity V_T, vertical air velocity V_A, particle mean diameter D_M, particle total number concentration N_T, liquid water content LWC, and rain rate R_R, respectively, for cloud. (a2-f2) are the same meaning as (a1-f1), but for precipitation.

3.5. Particle size distributions of warm cloud and precipitation

Particle size distributions of cloud and precipitation are vital information for numerical models. The MMCR can simultaneously derive high-spatiotemporal resolution of particle diameter and number concentration from Doppler spectra. However, as shown in Figure 15, the cloud droplets smaller than 0.12 mm are unavailable because of the limitation of radar sensitivity. Therefore, herein, particle size distributions only for large cloud droplets and raindrops are mainly concerned. Note that the above mentioned CBH-based classification approach of cloud and precipitation can misclassify a partial of particles and cause unideal statistical results of cloud and precipitation. Thus, the particles in both cloud and precipitation can be contaminated by each other to some extent.

Figure 16 (a) and (b) present the radar-derived mean particle size distributions of cloud and precipitation in five Z regimes. It can be seen that the particle spectra in cloud and precipitation gradually becomes wider with both increases of particle size and number concentration as radar-measured Z increases. The cloud owns narrower spectra than the precipitation, for the number concentration greater than 1 m^{-3}·mm^{-1}, the particle diameter of cloud and precipitation in five Z regimes are within (0.12-0.54 mm, 0.12-0.64 mm, 0.12-0.73 mm, 0.12-0.86 mm, and 0.12-1mm) and

Peer-reviewed version available at Remote Sens. 2019, 11, 3045; doi:10.3390/rs11243045

(0.13-0.97 mm, 0.13-1.19 mm, 0.13-1.35 mm, 0.15-1.48 mm, and 0.15-1.84 mm), respectively, and their maximums of number concentrations are (7.7625×10^4 $m^{-3}\cdot mm^{-1}$, 1.6596×10^5 $m^{-3}\cdot mm^{-1}$, 1.7378×10^5 $m^{-3}\cdot mm^{-1}$, 2.3442×10^5 $m^{-3}\cdot mm^{-1}$, and 2.2909×10^5 $m^{-3}\cdot mm^{-1}$) and (7.9433×10^3 $m^{-3}\cdot mm^{-1}$, 3.02×10^4 $m^{-3}\cdot mm^{-1}$, 5.8884×10^4 $m^{-3}\cdot mm^{-1}$, 9.3325×10^4 $m^{-3}\cdot mm^{-1}$, and 1.1749×10^5 $m^{-3}\cdot mm^{-1}$), respectively. In addition, the derived particle size distributions of cloud and precipitation both seem to be exponential as a study by Marshall and Palmer [72]. Therefore, herein, the formulas of particle size distributions for warm cloud and precipitation in different reflectivity regimes are further fitted and proposed. The expression can be written as,

$$N(D) = \alpha \times \exp(\beta \times D) \quad (27)$$

where D (mm) is the particle diameter, N(D) ($m^{-3}\cdot mm^{-1}$) is the number concentration of the diameter D, α and β are the intercept and slope parameters. The fitting results are shown in Table 3. It presents that the particle size distribution in both warm cloud and precipitation can be quite well expressed by the exponential formula with high fitting rates within 0.82-0.9985.

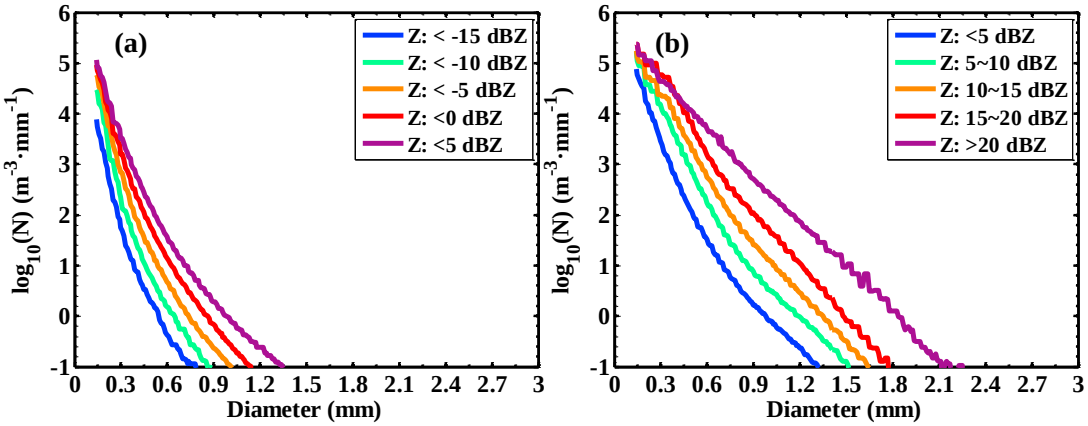

Figure 16. MMCR-retrieved mean particle size distribution of cloud (a) and precipitation (b) in five different Z regimes.

Table 3. The fitting results of particle size distribution expression $N(D) = \alpha \times \exp(\beta \times D)$ for warm cloud and precipitation.

Cloud				Precipitation			
Z (dBZ)	α	β	Fitting rate	Z (dBZ)	α	β	Fitting rate
< -15	6.841×10^5	-31.97	0.9985	< 5	5.747×10^5	-17.18	0.9463
< -10	1.874×10^6	-29.01	0.9851	5-10	5.138×10^5	-11.72	0.9036
< -5	2.202×10^6	-25.62	0.9656	10-15	4.481×10^5	-9.587	0.854
< 0	1.927×10^6	-22.1	0.9284	15-20	6.498×10^5	-8.126	0.82
< 5	1.629×10^6	-19.59	0.9122	>20	4.946×10^5	-7.504	0.9014

4. Discussion

As analyzed in subsection 3.4 and 3.5, the MMCR combined with ceilometer can separate the warm cloud and precipitation, which consist of cloud droplets and raindrops, respectively. However, a small part of hydrometeor is still unsuccessfully classified and can affect the statistical results of vertical structures and particle size distributions of cloud and precipitation. As shown in Figure 14-16, the related statistics of cloud and precipitation exhibit no clear boundaries. This deficiency may be caused by the measuring bias of ceilometer CBH, which misclassifies a part of raindrops as cloud droplets, as well as mistakes a part of cloud droplets as raindrops. In addition, some low-level weak targets detected by the MMCR, such as clutter, turbulence, fog and et al., which lie under the ceilometer-measured CBH, can also be incorrectly misclassified as raindrops. Therefore, herein,

Peer-reviewed version available at Remote Sens. 2019, 11, 3045; doi:10.3390/rs11243045

MMCR-derived particle size distributions under CBH (150-300 m) in different Z regimes are further compared with the disdrometer measurements in order to discuss the misclassification of precipitation and verify the reliability of MMCR-derived result. The comparisons are shown in Figure 17, which indicate that: (I) despite a much higher resolution of MMCR, the derived particle size distribution with no Z limitations [Figure 17 (a)] is different with the disdrometer measurement, the former presents higher/lower number concentrations as the particle diameter less/greater than 0.4 mm. (II) While, for the results in the posterior four Z regimes as drawn in Figure 17 (b-f), the radar gradually draws near to the disdrometer as Z increase from 5 to 20 dBZ. Especially for Z within 15-20 dBZ, the radar result is quite well with small deviations compared with the disdrometer counterparts. For Z greater than 20 dBZ, the radar result is more fluctuant because of the decrease of data volume. (III) For large raindrops, the radar-derived result underestimates the number concentration because of the limitation of signal attenuation and oversaturation at low levels. However, for the small targets, such as the particles in the first and second diameter channels of disdrometer, as shown in Figure (a-d), the radar-derived number concentrations of targets are greater than the reality of raindrops, indicating that the radar retrievals contain some contaminations induced by the non-rainfall targets. Furthermore, it can be found that the contamination seems to be disappeared as Z increasing to 15 dBZ, under which reflectivity the radar signal impossibly contains a noticeable part of the non-raindrop weak targets.

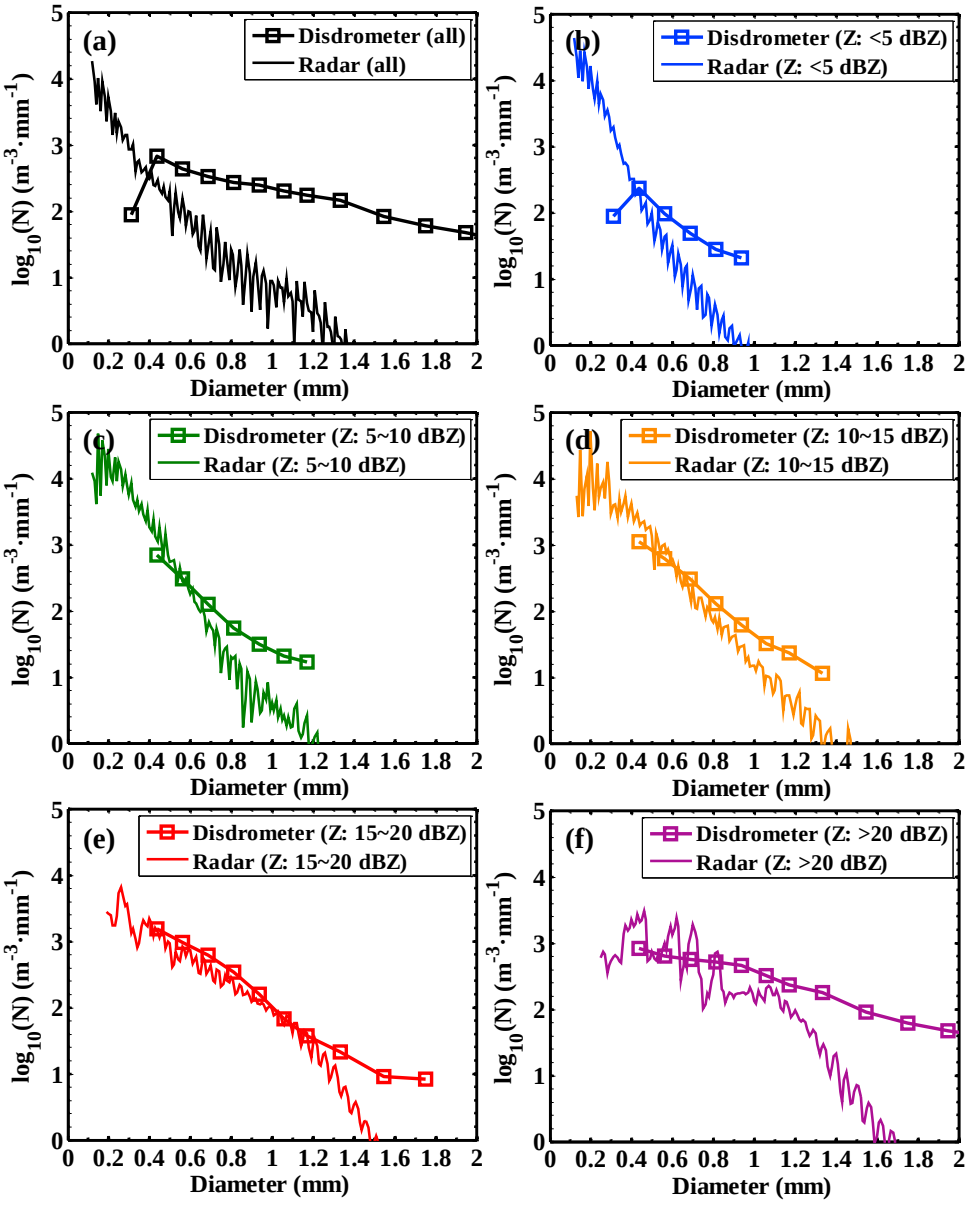

Peer-reviewed version available at Remote Sens. 2019, 11, 3045; doi:10.3390/rs11243045

Figure 17. Comparisons of MMCR-retrieved (150-300 m) and disdrometer-measured (on the ground) mean particle size distributions of precipitation in five different Z regimes.

5. Conclusions

The vertically pointing Ka-MMCR in conjunction with the laser ceilometer and disdrometer provides continuous and high-spatiotemporal-resolution measurements of cloud-precipitation. In this paper, appropriate data processing, quality control and retrieval technologies for the MMCR and disdrometer were presented to improve the data quality and obtain additional macrophysical and microphysical parameters of cloud-precipitation. Subsequently, 18 kinds of quantities of these three instruments were used to study the distribution, diurnal variation, vertical structure, and physical property of warm cloud-precipitation in South China during the pre-flood season.

The results showed that the proposed technologies can eliminate the plankton target contamination and alleviate signal attenuation of MMCR, and correct overestimation and remove the problematic data of disdrometer. The occurrence of aloft warm cloud-precipitation gradually decreased as height increased, and most of hydrometeors were concentrated below 2 km. The ground rainfall was dominated by light precipitation most of the time. However, short-time strong showers contributed to the majority of rain amounts. The cloud mostly had base heights below 2.2 km, thicknesses thinner than 2.1 km, and decentralized top heights within 0.6-4.2 km. Most of cloud-precipitation with 76.1% were single-layer, 20.6% and 3.29% were double-layer and triple-layer. The cloud-precipitation had certain diurnal variations. The cloud base height had a rising trend during the afternoon and midnight because of solar radiation heating. Convections were more frequent during three periods, namely, 0230-1100, 1200-1800, and 2100-2300, with higher cloud tops, thicker cloud thickness, higher rainfall occurrences, stronger radar reflectivity, larger hydrometeors, higher concentrations, faster particle terminal velocities, larger water contents, and stronger rain rates. At other times, the convections were relatively rare and weak.

Cloud and precipitation were separated and dividedly calculated. The results indicated that they had different vertical structures and physical properties, exhibiting different value ranges and changes along with heights of radar reflectivity, terminal falling velocity, vertical air motion, particle size, particle number concentration, liquid water, and rain rate. It was also found that air motions in warm cloud and precipitation were both weak, the updrafts mainly occurred in the low level and weakened along with height by rainfall scour, the downdraft gradually increased as height decreased attributed to the rainfall drag and evaporation effects. For physical processes, the cloud particle spectrum changed more moderately along with height than the precipitation, with the particle growth process mainly occurred in the middle part of cloud body. In contrast, the collision and coalescence processes of raindrops in precipitation were more rapidly, especially in a 2-km falling path near the ground. The particle size distributions of warm cloud and precipitation can both be well fitted by exponential expressions.

Verification of radar-retrieved raindrop size distribution showed that the radar result was very coherent with the ground measurement when the reflectivity of precipitation was within 10-20 dBZ. However, for other reflectivity regimes, radar retrievals underestimated large raindrops and overestimated small raindrops, as a result of reasons, including differences in instruments' sensitivity and sampling height, contamination of other non-precipitating weak targets, and attenuation under strong rainfall condition.

Author Contributions: Conceptualization, J.Z. and L.L.; methodology, J.Z.; software, J.Z., H.C.; validation, H.C. and Y.G.; formal analysis, Y.C.; investigation, J.Z.; resources, L.L.; data curation, J.Z. and L.L.; writing—original draft preparation, J.Z.; writing—review and editing, Y.C., H.C., and Y.G.; visualization, Q.L.; supervision, H.X.; project administration, J.Z.; funding acquisition, J.Z.

Funding: This research was funded by the Major Research Plan of the National Natural Science Foundation of China (Grant No. 91537214), the National Natural Science Foundation of China (Grant Nos. 41705008, 41905084), and the Scientific Research Foundation of Chengdu University of Information Technology (Grant No. KYTZ201728).

Peer-reviewed version available at Remote Sens. 2019, 11, 3045; doi:10.3390/rs11243045

Acknowledgments: The authors would like to thank the Chinese Academy of Meteorological Sciences for providing the radar data. Thanks also go to the reviewers for thorough comments that really helped to improve the manuscript.

Conflicts of Interest: The authors declare no conflict of interest.

Appendix A

Table A. Abbreviations used in this paper

No.	Abb.	Meaning	No.	Abb.	Meaning
1	MMCR	millimeter-wave cloud radar	13	K_T	spectral kurtosis
2	SP	Doppler spectrum	14	CTK	cloud thickness
3	Z	reflectivity	15	CLN	cloud layer number
4	V_M	mean Doppler velocity	16	V_A	vertical air velocity
5	S_w	spectrum width	17	V_T	particle mean terminal velocity
6	LDR	linear depolarization ratio	18	D_M	particle mean diameter
7	CBH	cloud base height	19	N_T	particle total number concentration
8	CTH	cloud top height	20	LWC	liquid water content
9	DSD	drop size distribution	21	LM,	Longmen weather observatory
10	R_R	rain rate	22	V_f	falling velocity
11	R_M	rain amount	23	QC	quality control
12	S_K	spectral skewness			

References

1. Beard, K.V.; Ochs, H.T. Warm Rain Initiation: An Overview of Microphysical Mechanisms. *J.Appl.Meteor.* **1993**, 32, 608-625. https://doi.org/10.1175/1520-0450(1993)032<0608:WRIAOO>2.0.CO;2
2. Hartmann, D.L.; Ockert-Bell, M.E.; Michelsen, M.L. The Effect of Cloud Type on Earth's Energy Balance: Global Analysis. *J. Clim.* **1992**, 5, 1281-1304.
3. Petty, G.W. Prevalence of Precipitation from Warm-Topped Clouds over Eastern Asia and the Western Pacific. *J. Clim.* **1999**, 12, 220-229. https://doi.org/10.1175/1520-0442-12.1.220
4. Kodama, Y.M.; Katsumata, M.; Mori, S.; Satoh, S.; Hirose, Y.; Ueda, H. Climatology of Warm Rain and Associated Latent Heating Derived from TRMM PR Observations. *J. Clim.* **2009**, 22, 4908-4929. Doi: 10.1175/2009JCLI2575.1
5. Narendra Reddy, N.; Venkat Ratnam, M.; Basha, G.; Ravikiran, V. Cloud Vertical Structure over A Tropical Station Obtained Using Long-term High-resolution Radiosonde Measurements. *Atmos. Chem. Phys* **2018**, 18, 11709-11727. https://doi.org/10.5194/acp-18-11709-2018
6. Chen, S.S.; Kerns, B.W.; Guy, N.; Jorgensen, D.P.; Savarin, A. Aircraft Observations of Dry Air, the ITCZ, Convective Cloud Systems, and Cold Pools in MJO during DYNAMO. *Bull. Am. Meteorol. Soc.* **2016**, 97, 405–423. DOI: 10.1175/BAMS-D-13-00196.1
7. Mcgill, M.; Hlavka, D.; Hart, W.; Scott, V.S.; Schmid, B. Cloud Physics Lidar: Instrument Description and Initial Measurement Results. *Applied Optics* **2002**, 41, 3725-3734. https://doi.org/10.1364/AO.41.003725
8. Yang, Y.J.; Lu, D.R.; Fu, Y.F.; Chen, F.J. Wang. Spectral Characteristics of Tropical Anvils Obtained by Combining TRMM Precipitation Radar with Visible and Infrared Scanner Data. *Pure Appl. Geophys.* **2015**, 172, 1717-1733. Doi: 10.1007/s00024-014-0965-x
9. Poore, K.D.; Wang, J.; Rossow, W.B. Cloud Layer Thicknesses from a Combination of Surface and Upper-Air Observations. *J. Clim.* **1995**, 8, 550-568. https://doi.org/10.1175/1520-0442(1995)008<0550:CLTFAC>2.0.CO;2
10. Sun, B.; Karl, T.R.; Seidel, D.J. Changes in Cloud-Ceiling Heights and Frequencies over the United States since the Early 1950s. *J. Clim.* **2007**, 20, 3956–3970. https://doi.org/10.1175/JCLI4213.1
11. Faccani, C.; Rabier, F.; Fourrié, N.; Agusti-Panareda, A.; Karbou, F.; Moll, P.; Lafore, J.-P.; Nuret, M.; Hdidou, F.; Bock, O. The Impacts of AMMA Radiosonde Data on the French Global Assimilation and Forecast System. *Wea. Forecasting* **2009**, 24, 1268-1286. 10.https://doi.org/10.1175/2009WAF2222237.1

Peer-reviewed version available at Remote Sens. 2019, 11, 3045; doi:10.3390/rs11243045

12. Wang, Z.; Wang, Z. H.; Cao, X. Z. Consistency analysis for cloud vertical structure derived from millimeter cloud radar and radiosonde profiles. *Acta Meteoro. Sin.* **2016**, 74, 1268-1286. https://doi.org/10.1016/j.atmosres.2017.09.009
13. Guo, J.; Miao,Y.; Zhang,Y.; Liu,H.; Li, Z.; Zhang, W.; He,J., Lou, M.; Yan, Y.;Bian, L.; Zhai, P. The Climatology of Planetary Boundary Layer Height in China Derived from Radiosonde and Reanalysis Data. *Atmos. Chem. Phys* **2016**, 16, 13309-13319. Doi: 10.5194/acp-16-13309-2016
14. Zhang, W.; Guo, J.; Miao, Y.; Liu, H.; Li, Z.; Zhai, P. Planetary Boundary Layer Height from CALIOP Compared to Radiosonde over China. *Atmos. Chem. Phys* **2016**, 16, 1-31. https://doi.org/10.5194/acp-16-9951-2016
15. Parish, T.R.; Rahn, D.A.; Leon, D. Aircraft Observations of A Coastally Trapped Wind Reversal off the California Coast. *Mon. Wea. Rev.* **2008**, 136, 644-662. https://doi.org/10.1175/2007MWR2199.1
16. Parish, T.R.; Leon, D. Measurement of Cloud Perturbation Pressures Using an Instrumented Aircraft. *J. Atmos. Ocean. Tech.* **2013**, 30, 215-229. https://doi.org/10.1175/JTECH-D-12-00011.1
17. Lawson, R.P.; Baker, B.A.; Schmitt, C.G.; Jensen, T.L. An Overview of Microphysical Properties of Arctic Clouds Observed in May and July 1998 during FIRE ACE. *J. Geophys. Res.* **2001**, 106, 14989-15014. https://doi.org/10.1029/2000JD900789
18. Hallett, J.; Isaac, G.A. Aircraft Icing in Glaciated and Mixed Phase Clouds. *J. Aircraft* **2008**, 45, 2120-2130. https://doi.org/10.2514/1.37596
19. Field, P.R.; Furtado, K. How Biased Is Aircraft Cloud Sampling?. *J. Atmos. Ocean. Tech.* **2016**, 33, 185-189. https://doi.org/10.1175/JTECH-D-15-0148.1
20. Houze, R.A. 100 Years of Research on Mesoscale Convective Systems. *Meteor. Monogr.* **2018**, 1. https://doi.org/10.1175/AMSMONOGRAPHS-D-18-0001.1
21. Chen, D.D.; Guo, J.P.; Wang, H.Q.; Li, J.; Min, M.; Zhao, W.H.; Yao, D. The Cloud Top Distribution and Diurnal Variation of Clouds over East Asia: Preliminary Results from Advanced Himawari Imager. *J. Geophys. Res. Atmos.* **2018**, 123, 3724-3739. https://doi.org/10.1002/2017JD028044
22. Painemal, D.; Minnis, P.; O'Neil, L. The Diurnal Cycle of Cloud-top Height and Cloud Cover over the Southerstern PACIFIC AS Observed by GOES-10. *J. Atmos. Sci.* **2013**, 70, 2393-2408. https://doi.org/10.1175/JAS-D-12-0325.1
23. Lu, F.; Zhang, X.; Xu, J. Image Navigation for the FY2 Geosynchronous Meteorological Satellite. *J. Atmos. Ocean. Tech.* **2008**, 25, 1149-1165. https://doi.org/10.1175/2007JTECHA964.1
24. Jun, Y.; Zhang, Z.Q.; Wei, C.Y.; Lu, F.; Guo, Q. Introducing the New Generation of Chinese Geostationary Weather Satellites, Fengyun-4. *Bull. Amer. Meteor. Soc.* **2017**, 98, 1637-1658. https://doi.org/10.1175/BAMS-D-16-0065.1
25. Liu, L.; Ruan, Z.; Zheng, J.; Gao, W. Comparing and Merging Observation Data from Ka-band Cloud Radar, C-band Frequency-modulated Continuous Wave Radar and Ceilometer Systems. *Remote Sens.* **2017**, 9, 1282. Doi: 10.3390/rs9121282
26. Wang, T.; Luo, J.; Liang, J.; Wang, B.; Tian, W.; Chen, X. Comparisons of AGRI/ FY-4A, Cloud Fraction and Cloud Top Pressure with MODIS/ Terra, Measurements over East Asia. *J. of Meteor. Res.* **2019**, 33, 705-719.
27. Wang, Z.H.; Wang, X.Z.; Cao, F.; Tao. Comparison of Cloud Top Heights derived from FY-2 Meteorological Satellites with Heights derived from Groud-based Millimeter Wavelength Cloud Radar. *Atmos. Res.* **2018**, 199, 113-127. https://doi.org/10.1016/j.atmosres.2017.09.009
28. Simpson, J. The Tropical Rainfall Measuring Mission (TRMM). *Meteor. Atmos. Phys.* **1988**, 60, 19-36. https://doi.org/10.1016/0273-1177(94)90210-0
29. Stephens, G.L.; Vane, D.G.; Boain, R.; Mace, G.; Sassen, K.; Wang, Z.; Illingworth, A.J.; Ewan, J.; O'connor, E.; Rossow, W.; Durden, S.L.; Durden, S.L.; Miller, S.; Austin, R.; Benedetti, A.; Mitrescu, C.; the CloudSat Science Team. The Cloudsat Mission and the EOS Constellation: A New Dimension of Space-Based Observation of Clouds and Precipitation. *Bull. Amer. Meteor. Soc.* **2002**, 83, 1771-1790.
30. Hou, A.Y.; Skofronick-Jackson, G.; Stocker, E.F. The Global Precipitation Measurement (GPM) Mission: Overview and U.S. Science Status. *Bull Amer Meteor Soc.* **2014**, 95, 701-722. Doi: 10.1175/BAMS-D-13-00164.1
31. Chen, H.; Chandrasekar, V.; Tan, H.; Cifelli, R. Rainfall Estimation from Ground Radar and TRMM Precipitation Radar Using Hybrid Deep Neural Networks. *Geophys. Res. Lett.* **2019**,46. https://doi.org/10.1029/

Peer-reviewed version available at Remote Sens. 2019, 11, 3045; doi:10.3390/rs11243045

32. Hagihara, Y.; Okamoto, H.; Luo, Z.J. Joint analysis of cloud-top heights from CloudSat and CALIPSO: New Insights into Cloud-top Microphysics. *J. Geophys. Res.* **2014**, 119, 4087-4106. https://doi.org/10.1002/2013JD020919
33. Protat, A.; Delanoë, J.; O'Connor, E.J.; L'Ecuyer T.S. The Evaluation of Cloud Sat and CALIPSO Ice Microphysical Products Using Ground-Based Cloud Radar and Lidar Observations. *J. Atmos. Ocean. Tech.* **2010**, 27, 793-810. Doi:10.1175/2009JTECHA1397.1.
34. Gorgucci, E.; Baldini, L. Performance Evaluations of Rain Microphysical Retrieval Using Gpm Dual-Wavelength Radar by Way of Comparison With the Self-Consistent Numerical Method. *IEEE Trans. Geosci. Remote Sens.* **2018**, 56, 5705 - 5716. 10.1109/TGRS.2018.2824399
35. Ni, X.; Liu, C.; Zipser, E. Ice Microphysical Properties near the Tops of Deep Convective Cores Implied by the GPM Dual-Frequency Radar Observations. *J. Atmos. Sci.* **2019**,76, 2899–2917. https://doi.org/10.1175/JAS-D-18-0243.1
36. Palerme, C.; Genthon, C.; Claud, C.; Kay, J.E.; Wood, N.B. L'Ecuyer, Tristan. Evaluation of Current and Projected Antarctic Precipitation in Cmip5 Models. *Climate Dyn.* **2017**, 48, 225-239.DOI: 10.1007/s00382-016-3071-1
37. Matrosov, S.Y. CloudSat Measurements of Landfalling Hurricanes Gustav and Ike (2008). *J. Geophys. Res.* **2012**, 116, D01203. https://doi.org/10.1029/2010JD014506
38. Jiang, X.; Waliser, D.E.; Li, J.L.; Woods, C. Vertical Cloud Structures of the Boreal Summer Intraseasonal Variability based on Cloudsat Observations and Era-interim Reanalysis. *Climate Dyn.* **2011**, 36, 2219-2232.
39. Takahashi, H.; Luo, Z.J. Characterizing Tropical Overshooting Deep Convection from Joint Analysis of CloudSat and Geostationary Satellite Observations. *J. Geophys. Res.* **2014**, 119, 112-121. Doi:10.1002/2013JD020972
40. Mace, G.G.; Marchand, R.; Zhang, Q.; Stephens, G. Global Hydrometeor Occurrence as Observed by CloudSat: Initial Observations from Summer 2006. *Geophys. Res. Lett.* **2007**, 34. https://doi.org/10.1029/2006GL029017
41. Liu, D.; Liu, Q.; Liu, G.; Wei, J.; Deng, S.; Fu Y. Multiple Factors Explaining the Deficiency of Cloud Profiling Radar on Detecting Oceanic Warm Clouds. *J. Geophys. Res.* **2018**, 123, 8135–8158. https://doi.org/10.1029/
42. Moran, K.P.; Martner, B.E.; Post, M.J.; Kropfli, R.A.; Widener, K.B. An Unattended Cloud-Profiling Radar for Use in Climate Research. *Bull. Amer. Meteor. Soc.* **1998**, 79, 443-455. https://doi.org/10.1175/1520-0477(1998)079<0443:AUCPRF>2.0.CO;2
43. Kollias, P.; Albrecht, B. Vertical Velocity Statistics in Fair-Weather Cumuli at the ARM TWP Nauru Climate Research Facility. *J. Clim.* **2010**, 23, 6590-6604. https://doi.org/10.1175/2010JCLI3449.1
44. Kollias, P.; Rémillard, J.; Luke, E.; Szyrmer, W. Cloud radar Doppler spectra in drizzling stratiform clouds: 1. Forward modeling and remote sensing applications. *J. Geophys. Res.* **2011**, 116. Doi:10.1029/2010JD015237
45. Kollias, P.; Albrecht, B.A.; Lhermitte, R.A. Savtchenko. Radar Observations of Updrafts, Downdrafts, and Turbulence in Fair-Weather Cumuli. *J. Atmos. Sci.* **2001**, 58, 1750-1766. https://doi.org/10.1175/1520-0469(2001)058<1750:ROOUDA>2.0.CO;2
46. Liu, L.; Ding, H.; Dong, X.; Cao, J.; Su, T. Applications of QC and Merged Doppler Spectral Density Data from Ka-Band Cloud Radar to Microphysics Retrieval and Comparison with Airplane in Situ Observation. *Remote Sens.* **2019**,11, 1595. https://doi.org/10.3390/rs11131595
47. Stokes, G.M.; Schwartz, S.E. The Atmospheric Radiation Measurement (ARM) Program: Programmatic Background and Design of the Cloud and Radiation Test Bed. *Bull. Amer. Meteor. Soc.* **1994**, 75, 1201–1221. https://doi.org/10.1175/1520-0477(1994)075<1201:TARMPP>2.0.CO;2
48. Zhao, P.; Xu, X.; Chen, F.; Guo, X.; Zheng, X.; Liu, L.; Hong, Y.; Li, Y.; La, Z.; Peng, H.; Zhong, L.; Ma, Y.; Tang, S.; Liu, Y.; Liu, H.; Li, Y.; Zhang, Q.; Hu, Z.; Sun, J.; Zhang, S.; Dong, L.; Zhang, H.; Zhao, Y.; Yan, X.; Xiao, A.; Wan, W.; Liu, Y.; Chen, J.; Liu, G.; Zhaxi, Y.; Zhou, X. The Third Atmospheric Scientific Experiment for Understanding the Earth–Atmosphere Coupled System over the Tibetan Plateau and Its Effects. *Bull. Amer. Meteor. Soc.* **2018**, 99, 757–776.
49. Illingworth, A.J.; Hogan, R.J.; O'Connor, E.; Bouniol, D.; Brooks, M.E.; Delanoé, J.; Donovan, D.P.; Eastment, J.D.; Gaussiat, N.; Goddard, J.W.; Haeffelin, M.; Baltink, H.K.; Krasnov, O.A.; Pelon, J.; Piriou, J.; Protat, A.; Russchenberg, H.W.; Seifert, A.; Tompkins, A.M.; Zadelhoff, G.V.; Vinit, F.; Willén, U.; Wilson, D.R.; Wrench, C.L. Cloudnet. *Biomechanical Engineering of Textiles & Clothing* **2007**, 88, 145–159. Doi: 10.1175/BAMS-88-6-883

Peer-reviewed version available at Remote Sens. 2019, 11, 3045; doi:10.3390/rs11243045

50. Zhang, Y.; Zhou, Q.; Lv, S.; Jia, S.; Tao, F.; Chen, D.; Guo, J. Elucidating Cloud Vertical Structures based on Three-year Ka-band Cloud Radar Observations from Beijing, China. *Atmos. Res.* **2019**, 222, 88-99. https://doi.org/10.1016/j.atmosres.2019.02.007
51. Chen, B.; Hu, Z.; Liu, L.; Zhang, G. Raindrop Size Distribution Measurements at 4,500 m on the Tibetan Plateau During TIPEX-III. *J. Geophys. Res. Atmos.* **2017**, 122, 11092-11106. Doi: 10.1002/2017JD027233
52. Clothiaux, E.E.; Ackerman, T.P.; Mace, G.G.; Moran, K.P.; Marchand, R.T.; Miller, M.A.; Martner, B.E. Objective Determination of Cloud Heights and Radar Reflectivities Using a Combination of Active Remote Sensors at the ARM CART Sites. *J. Appl. Meteorol.* **2000**, 39, 645-665. Doi: 10.1175/1520-0450(2000)039<0645:ODOCHA>2.0.CO;2
53. Feng, Z.; Sally, A.M.; Courtney, S.; Ellis, S.; Comstock, J.; Bharadwaj, N. Constructing a Merged Cloud–Precipitation Radar Dataset for Tropical Convective Clouds during the DYNAMO/AMIE Experiment at Addu Atoll. *J. Atmos. Ocean. Technol.* **2014**, 31, 1021-1042. https://doi.org/10.1175/JTECH-D-13-00132.1
54. Wang, H.; Kong, F.; Wu, N.; Lan, H.; Yin, J. An Investigation into Microphysical Structure of A Squall Line in South China Observed with A Polarimetric Radar and A Disdrometer. *Atmos. Res.* **2019,** 226, 171-180. https://doi.org/10.1016/
55. Luo, Y.; Zhang, R.; Wan, Q.; Wang, B.; Xiao, Y. The Southern China Monsoon Rainfall Experiment (SCMREX). *Bull. Amer. Meteor. Soc.* **2016**, 98, 999-1013. https://doi.org/10.1175/BAMS-D-15-00235.1
56. Huo, Z.; Ruan, Z.; Wei, M.; Wei, J.; Deng, S.; Fu,Y.F. Statistical Characteristics of Raindrop Size Distribution in South China Summer based on the Vertical Structure derived from VPR-CFMCW. *Atmos. Res.* **2019**, 222, 47-61. https://doi.org/10.1016/
57. Zheng, J.; Zhang, P.; Liu, L.; Liu, Y.; Che, Y. A Study of Vertical Structures and Microphysical Characteristics of Different Convective Cloud–Precipitation Types Using Ka-Band Millimeter Wave Radar Measurements. *Remote Sens.* **2019**, 11.
58. Liu, L.; Zheng, J. Algorithms for Doppler Spectral Density Data Quality Control and Merging for the Ka-Band Solid-State Transmitter Cloud Radar. *Remote Sens.* **2019**, 11, 209. https://doi.org/10.3390/rs11020209
59. Hildebrand, P.H.; Sekhon, R.S. Objective Determina-tion of the Noise Level in Doppler Spectra. *J. Appl. Meteor.* **1974**, 13, 808–811. https://doi.org/10.1175/1520-0450(1974)013<0808:ODOTNL>2.0.CO;2
60. Matrosov, S.Y. Attenuation-Based Estimates of Rainfall Rates Aloft with Vertically Pointing Ka-Band Radars. *J. Atmos. Ocean. Technol.* **2005**, 22, 43-54. https://doi.org/10.1175/JTECH-1677.1
61. Görsdorf, U.; Volker, L.; Matthias B.P.; Gerhard, P.; Dmytro, V.; Vladimir, V.; Vadim, V. A 35-GHz Polarimetric Doppler Radar for Long-Term Observations of Cloud Parameters—Description of System and Data Processing. *J. Atmos. Oceanic Technol.* **2015**, 32, 675–690. https://doi.org/10.1175/JTECH-D-14-00066.1
62. Luke, E.P.; Luke, E.P.; Kollias, P.; Johnson, K.L.; Clothiaux, E.E. A Technique for the Automatic Detection of Insect Clutter in Cloud Radar Returns. *J. Atmos. Oceanic Technol.* **2008**, 25, 1498-1513. https://doi.org/10.1175/2007JTECHA953.1
63. Jia-Feng, Z.; Li-Ping, L.; Zheng-Mao, Z.; Xiao-Lin, X.; Jing-Ya, W. U.; Kai, F. Ka-band Millimeter Wave Cloud Radar Data Quality Control. *J. Infrared Millim. Waves* **2016**, 35, 748~757. Doi: 10.11972/j.issn.1001-9014.2016.06.018
64. Gossard, E.E. Measurement of Cloud Droplet Size Spectra by Doppler Radar. *J. Atmos. Ocean. Technol.* **1994**, 11, 712-726. https://doi.org/10.1175/1520-0426(1994)011<0712:MOCDSS>2.0.CO;2
65. Kollias, P.; Albrecht, B.A.; Lhermitte, R.; Savtchenko, A. Radar Observations of Updrafts, Downdrafts, and Turbulence in Fair-weather Cumuli. *J. Atmos. Sci.* **2001**, 58, 1750-1766. https://doi.org/10.1175/1520-0469(2001)058<1750:ROOUDA>2.0.CO;2
66. Shupe, M.D.; Kollias, P.; Matrosov, S.Y.; Schneider, T.L. Deriving Mixed-Phase Cloud Properties from Doppler Radar Spectra. *J. Atmos. Ocean. Technol.* **2004**, 21, 660-670. https://doi.org/10.1175/1520-0426(2004)021<0660:DMCPFD>2.0.CO;2
67. Jiafeng, Z.; Liping, L.; Keyun, Z.; Jingya, W.; Binyun, W. A Method for Retrieving Vertical Air Velocities in Convective Clouds over the Tibetan Plateau from TIPEX-III Cloud Radar Doppler Spectra. *Remote Sens.* **2017**, 9, 964. Doi: 10.3390/rs9090964
68. Sokol, Z.; Minářová, J.; Novák, P. Classification of Hydrometeors Using Measurements of the Ka-Band Cloud Radar Installed at the Milešovka Mountain (Central Europe). *Remote Sens.* **2018**, 10, 1674. https://doi.org/10.3390/rs10111674

Peer-reviewed version available at Remote Sens. 2019, 11, 3045; doi:10.3390/rs11243045

69. Gunn, R.; Kinzer, G.D. The Terminal Velocity of Fall for Water Droplets in Stagnant Air. *J. Meteorol.* **1949**, 6, 243-248. Doi: 10.1175/1520-0469(1949)006<0243:TTVOFF>2.0.CO;2
70. Foote, G.B.; Toit, P.S.D. Terminal Velocity of Raindrops Aloft. *J. Appl. Meteorol.* **1969**, 8, 249-253. https://doi.org/10.1175/1520-0450(1969)008<0249:TVORA>2.0.CO;2
71. Battaglia, A.; Rustemeier, E.; Tokay, A.; Blahak, U.; Simmer, C. PARSIVEL Snow Observations: A Critical Assessment. *J. Atmos. Ocean. Technol.* **2010**, 27, 333-344. https://doi.org/10.1175/2009JTECHA1332.1